Progress in Oceanography 105 (2012) 102–124

Contents lists available at SciVerse ScienceDirect

Progress in Oceanography

journal homepage: www.elsevier.com/locate/pocean

Validation of the Kuroshio Current System in the dual-domain Pacific Ocean Model framework

Yu-Heng Tseng [a,*], Mao-Lin Shen [a], Sen Jan [b], David E. Dietrich [c], Chia-Ping Chiang [a]

[a] Department of Atmospheric Sciences, National Taiwan University, Taipei, Taiwan
[b] Institute of Oceanography, National Taiwan University, Taipei, Taiwan
[c] AcuSea Inc., San Diego, USA

ARTICLE INFO

Article history:
Available online 25 April 2012

ABSTRACT

A fourth-order, fully two-way-coupled dual-domain Pacific Ocean Model (DUPOM) is developed to simulate the regional circulation in Asian Marginal Seas based on the whole North Pacific Ocean simulation framework. The model uses 1/4° and 1/8° horizontal resolutions for the eastern and western Pacific Ocean domains, respectively. The fully two-way-coupled approach shows seamless coupling behavior without any sponge layer. We validate the Kuroshio Current System and the regional circulation in the Asian Marginal Sea, including circulation patterns, volume transport variation and vertical current structure across several cross-sections. A single strong current core exists east of Taiwan and extends to the East China Sea. A cold dome near the northeast of Taiwan is a semi-permanent feature in the model results as observed. South of Japan (e.g. PCM5 line), the Kuroshio shows strong transport along the coast with a countercurrent offshore, reflecting a recirculation gyre. The transient of the three typical paths of the Kuroshio meander is also studied. Our results suggest that the path variation, particularly the Large Meander path, may be triggered by the baroclinic instability associated with westward propagating eddies.

1. Introduction

The major western boundary current in the North Pacific, the Kuroshio, transports enormous amounts of mass (e.g., geochemical materials) and energy (e.g., heat) from the low to mid-latitude regions. It affects not only global ocean climate variations but also the regional climate system in East Asia (e.g., Guo et al., 2002; Yoshinari et al., 2004). Particularly, the Kuroshio has various paths south of Japan, which strongly influence fisheries, ship navigation, marine resources, etc. Thus, its path, transport and dynamics are of great interest and have been studied extensively for many decades (e.g. Hsueh, 2000; Kawabe, 1995, 2005; McCreary and White, 1979; Miyazawa et al., 2008; Taft, 1972).

The Tokara Strait, located at around 30°N and 130°E with a northeast–southwest inclination, is the primary passage of the Kuroshio flowing from the ECS to the Pacific Ocean south of Japan (Nitani, 1972; Nagata and Takeshita, 1985). It may be regarded as a counterpart of the Florida Strait for the Gulf Stream system. The variability of the Kuroshio current axis position and the volume transport across Tokara Strait has been thought to be closely related to the path variation of the Kuroshio south of Japan. Early studies examined sea-level difference between Naze and Nishinoomote at the Tokara Strait from 1965 through 1983, and showed that the long-term mean semi-monthly velocity of the Kuroshio is fastest during July and slowest during the second half of October (Kawabe, 1988). Although the long term mean annual cycle current strength has a maximum in summer and a minimum in fall, significant inter-annual variability exists, and the only feature found every year is a weak velocity from September to December (Taft, 1972; Kawabe, 1988). Different estimates of the Kuroshio volume transport through Tokara Strait range from 18 to 32 Sv ($1\ \mathrm{Sv} \equiv 10^6\ \mathrm{m}^3/\mathrm{s}$) (Zhu et al., 2006).

The Kuroshio originates from the northward branch of the bifurcated North Equatorial Current (NEC) off the Philippine coast (Nitani, 1972), enters the East China Sea (ECS) through the passage east of Taiwan, and flows northeastward along the continental shelf in the ECS with a minor variation of its jet core. The main Kuroshio axis veers at around 30°N, 129°E and flows into the Tokara Strait, south of Kyushu, Japan (Fig. 1). After passing through the Tokara Strait, the Kuroshio intensifies and continues to flow along the southern coast of Japan, where it shows the well-known bimodal paths (Fig. 1c): the Large Meander (LM) path and the Non-Large Meander (NLM) path. The NLM path can be further categorized into nearshore non-large meander (nNLM) and offshore non-large meander (oNLM). It then leaves Honshu, Japan, off the Boso Peninsula and enters the Pacific Ocean as the Kuroshio Extension (KE).

Many early studies relate the variation between the LM and NLM paths to the condition of the Kuroshio south of Kyushu. It

* Corresponding author. Present address: Climate and Global Dynamics Division, National Center for Atmospheric Research, Boulder, USA.
E-mail address: ytseng@ucar.edu (Y.-H. Tseng).

0079-6611/$ - see front matter © 2012 Elsevier Ltd. All rights reserved.
http://dx.doi.org/10.1016/j.pocean.2012.04.003

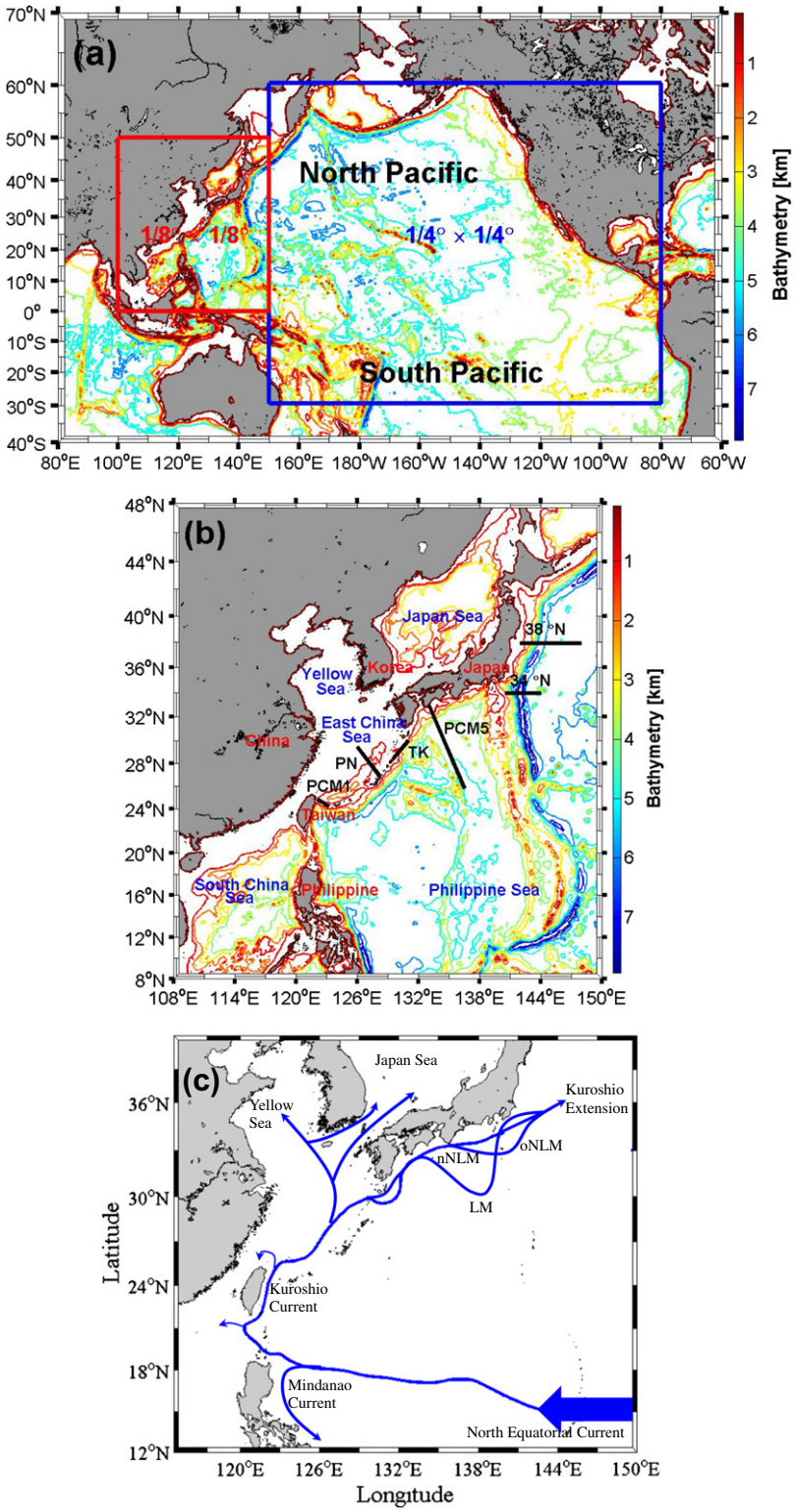

Fig. 1. (a) Schematic of the model domain. The eastern Pacific (NPB domain, horizontal grid resolution of 1/4°) is the block at the right while the western Pacific (TAI domain, horizontal grid resolution of 1/8°) is at the left. (b) The PCM-1, PN, TK, and PCM-5 (ASUKA) lines are marked. The contour interval of the bathymetry is 1 km. (c) The major current system of western North Pacific, including NEC, Kuroshio to Kuroshio Extension and its branches. Different meander paths are shown as nNLM, oNLN and LM, respectively.

was suggested that the volume transport of the Kuroshio through Tokara Strait could be regarded as an index for the formation of a LM path of the Kuroshio (Feng et al., 2000). Kawabe (1985, 1995, 2005) used sea level data to examine the variations of the (typical) path of the Kuroshio and their relations with current velocity, volume transport, and upstream position. Kawabe noted that the end points of the three typical paths (i.e., LM, nNLM and oNLM) are all near the same latitudes south of Japan at 131°E and 142°E. The nNLM and the oNLM paths overlap between Kyushu and the Kii Peninsula, being close to the south coast of Japan.

However, the typical LM locates offshore south of Shikoku, Japan. The Kuroshio takes an NLM path (either nNLM or oNLM) when the volume transport is small, while it is possible to take either a LM or a NLM path when the volume transport is in the range of medium to large. For the latter, a LM path occurs when the Kuroshio is in a northern position in the Tokara Strait south of Kyushu, Japan, which implies a small curvature and directly relates with the dynamics of a LM.

Further upstream of the Kuroshio, Ichikawa and Beardsley (2002) reviewed the current system in the ECS. Long-term hydrographic observations in the ECS have been made along the PN (Pollution Nagasaki) line by Nagasaki Marine Observatory of the Japan Meteorological Agency (JMA) since 1972. The geostrophic volume transport of the Kuroshio (northeastward velocity component), referenced to the 700-dbar level along section PN, has been used as an index of the long-term variation of the Kuroshio volume transport in the ECS. The long-term relative transport from 1973 to 2000 is 25.8 Sv, with a maximum mean of 27.0 Sv in summer and minimum of 23.9 Sv in autumn. Hinata (1996) suggested a slightly smaller mean geostrophic volume transport (25.4 Sv) with a little decrease in autumn based on the hydrographic data observed along the PN line from 1973 to 1993. Ichikawa and Chaen (2000) found that the seasonal mean volume transport of northeastward current through the PN section may vary from a minimum of 20.0 Sv in winter to a maximum of 32.1 Sv in summer with an annual mean of 27.6 Sv, by integrating the geostrophic volume transport or ship-mounted ADCP velocity in each transect during 1981–1992.

Historical hydrographic observation indicates a cold upwelling center is usually observed northeast of Taiwan (Tang et al., 2000), accompanied with a cyclonic eddy (Chuang et al., 1993; Hsueh, 2000). Chern and Wang (1989) found the upwelling subsurface water intruded northwestwardly onshore and into the ECS to form the Taiwan Warm Current. The China Coastal Water also flows equatorward into the Taiwan Strait (TS) with its branches extending to the north coast of Taiwan. The cold dome results from the upwelling of subsurface Kuroshio water (Chen et al., 1995), which is possibly caused by the effect of topography, monsoon, and current meander (Yin, 1973; Fan, 1980; Lin et al., 1992). The cold watermass is characterized by low temperature, high salinity, high density, low dissolved oxygen, high phosphate, high silicate, and high nitrate.

The main objective of this paper is to validate the mean structure of the Kuroshio Current System (KCS) in the Asian Marginal Seas and its variation based on the recently developed, multi-scale duo-grids Pacific Ocean Model (DUPOM), which is a standard configuration of the Taiwan Multi-scale Community Ocean Model (TIMCOM). The model is downloadable from http://efdl.as.ntu.edu.tw/research/timcom (Young et al., 2012). Fig. 1c shows the major KCS and its branches in the Asian Marginal Seas. Hurlburt et al. (1996) demonstrated that higher resolution greatly improves the upper-ocean circulation of the KCS to properly resolve the Rossby radius (~30 km) and the amplitude of mesoscale fluctuations due to baroclinic instabilities. The DUPOM uses finer grid near the continental shelf in the western domain to resolve the smaller Rossby radius and coarser grid in the eastern one, which provides the resolution required, while maintaining minimum computational cost and highest efficiency. The eddy-resolving DUPOM particularly emphasizes the key features of the KCS in the North Pacific and serves as an important benchmark/validation of the continuous eddy-resolving global ocean model development. Furthermore, the commonly observed cold dome in the northeast of Taiwan is addressed and some possible formation mechanisms are proposed. Finally, the variation and instability of the Kuroshio meander path south of Japan are discussed, based on the model results. Some processes or mechanisms which may contribute to the LM are also investigated. This paper is organized as follows. Section 2 introduces the governing equations and the multi-scale DUPOM. Section 3 provides the general description and comparison with observation data along several cross-sections. Section 4 discusses the appearance of the cold dome northeast of Taiwan. Section 5 analyzes the typical paths of the Kuroshio south of Japan and the generation of the LM in the model. Finally, conclusions are drawn in Section 6.

2. Model description and duo-grid coupling

In order to accurately investigate the regional circulation in the Western North Pacific, we used a hydrostatic, z-level, fourth-order accurate DUPOM, which provides high computational accuracy and low numerical dissipation and dispersion (Dietrich et al., 2004, 2008; Tseng et al., 2005).

2.1. Governing equations

The governing equations are based on the three-dimensional (3D) primitive equations for an incompressible, stratified fluid in the spherical coordinate. We describe the hydrostatic model using the rigid-lid and Boussinesq approximations. λ is the longitudinal variable, φ is the latitudinal variable, and z is the vertical variable, respectively.

- Conservation of mass:

$$\frac{1}{R\cos\phi}\left(\frac{\partial u}{\partial\lambda}+\frac{\partial(v\cos\phi)}{\partial\phi}\right)+\frac{\partial w}{\partial z}=0, \tag{1}$$

- Horizontal momentum equations:

$$\frac{\partial u}{\partial t}=-Lu+\left(f+\frac{u\tan\phi}{R}\right)v-\frac{1}{\rho_0 R\cos\phi}\frac{\partial p}{\partial\lambda}+D_m u+\frac{\partial}{\partial z}\left(A_u\frac{\partial u}{\partial z}\right), \tag{2}$$

$$\frac{\partial v}{\partial t}=-Lv-\left(f+\frac{u\tan\phi}{R}\right)u-\frac{1}{\rho_0 R}\frac{\partial p}{\partial\phi}+D_m v+\frac{\partial}{\partial z}\left(A_v\frac{\partial v}{\partial z}\right), \tag{3}$$

- Conservation of potential temperature:

$$\frac{\partial T}{\partial t}=-LT+D_h T+\frac{\partial}{\partial z}\left(K_T\frac{\partial T}{\partial z}\right), \tag{4}$$

- Conservation of dissolved salt:

$$\frac{\partial S}{\partial t}=-LS+D_h S+\frac{\partial}{\partial z}\left(K_S\frac{\partial S}{\partial z}\right), \tag{5}$$

- Hydrostatic equation:

$$\frac{\partial p}{\partial z}=-(\rho-\bar{\rho})g, \tag{6}$$

- Equation of state:

$$\rho=\rho(S,T,p), \tag{7}$$

where u and v are the velocity components in λ and ϕ direction, respectively, and w is vertical velocity. S is the salinity and T is the potential temperature. f is the Coriolis parameter; ρ_0 is the mean density; $\bar{\rho}$ is the horizontal average of density at depth z; p is the pressure. A_u and A_v are vertical eddy viscosity coefficients for horizontal momentum equations while K_s and K_T are the vertical eddy diffusivity for salinity and temperature equations. The convection and horizontal diffusion operators L, $D_{m(h)}$ are defined as:

$$L = \frac{u}{R\cos\phi}\frac{\partial}{\partial\lambda} + \frac{v}{R}\frac{\partial}{\partial\phi} + w\frac{\partial}{\partial z},$$

$$D_{m(h)} = \frac{1}{R^2}\left(\frac{1}{\cos^2\phi}\frac{\partial^2}{\partial\lambda^2}A_{m(h)} - \tan\phi\frac{\partial}{\partial\phi}A_{m(h)} + \frac{\partial^2}{\partial\phi^2}A_{m(h)}\right),$$

where $A_{m(h)}$ is the location-dependent horizontal eddy viscosity (diffusivity) coefficient for momentum (or scalar) equations. Assuming that the hydrostatic approximation is valid, the pressure field can be computed by integrating (6) from rigid-lid surface to any depth z:

$$p = p_s + p_b, \quad p_b = g\int_z^0 \rho dz,$$

where p_s is the surface pressure due to atmospheric or other physical phenomena.

2.2. Model description

Our model domain covers the entire North Pacific Ocean ranging from 100°E to 80°W and from 30°S to 60°N (see Fig. 1a for the model domain and the bathymetry). To reduce the computational time, we use a duo-grid approach based on the multiple-grid framework (Dietrich et al., 2004, 2008). A 1/4° horizontal resolution is used east of 150°E (right blue block in Fig. 1a, i.e., the NPB domain), while a finer horizontal resolution of 1/8° is used west of 150°E (left red block in Fig. 1a, i.e., the TAI domain) where the detailed Kuroshio and the associated circulations in the marginal seas are adequately resolved.

Model bathymetry is interpolated from unfiltered ETOPO-2 depth data[1] supplemented with Taiwan's National Center for Ocean Research's (NCOR) 1-min high accuracy depth archive in the Asian Seas (Liu et al., 1998). The vertical resolution is a linear-exponential stretched grid of 25 layers with a thickness of 10 m in the top layer. Both domains use the same vertical grids to avoid inconsistency. Within each domain, longitudinal resolution is uniform and latitudinal resolution is generated such that varying latitude and longitude grid increments are equal everywhere (Mercator grid). The time step is 200s and 600s for the TAI and NPB domains respectively. The surface wind forcing is obtained from the interpolated monthly Hellerman and Rosenstein winds stress (Hellerman and Rosenstein, 1983). The Levitus 94 seasonal climatology (Levitus and Boyer, 1994) is used to initialize the model and determine its surface sources of heat and fresh water using the non-damping precise approach. Since the main purpose of this study is to validate the general patterns of the KCS in the Asian Marginal Seas in the climatological time scale, the monthly HR wind stresses and Levitus 94 are good enough to resolve the important features for the validation. More realistic surface forcing such as QuitSCAT is also used to simulate the oceanic response to typhoons based on this framework (e.g., Tseng et al., 2010). The horizontal heat and momentum diffusivities are set to be 10^6 cm^2/s and 2×10^5 cm^2/s, respectively. Augmented molecular viscosity and diffusivity are determined by parameterized synoptic wind events, and by breaking (u, v, T, S, near surface only) and non-breaking (u, v only, at all levels) internal waves. The vertical mixing is parameterized by eddy diffusivity (for temperature and salinity) and viscosity (for momentum) using a modified Richardson number dependent formula based on Pacanowski and Philander (Pacanowski and Philander, 1981; Tseng et al., 2005). For the TAI domain, both northern and southern boundaries are closed. For the NPB domain, the northern boundary is closed and the southern boundary condition (30°S) is slowly nudging toward climatology in a sponge layer. The bottom is insulated, with non-slip conditions parameterized by a non-linear bottom drag. The zonal boundary exchanges are detailed in the next section and more discussion about the open boundary treatment can be found in Tseng et al. (2005).

2.3. Energy conservative two-way coupling: algorithm

The DUPOM takes advantage of the fully two-way coupling approach from the earlier multiple-grid Mediterranean Sea/North Atlantic model framework (Dietrich et al., 2008). This approach is different from the parallel domain-decomposed TIMCOM which is more useful for the global ocean simulation in the uniform resolution (Tseng and Chien, 2011). Within each individual grid (all in a spherical coordinate framework), longitudinal resolution is uniform and latitudinal resolution is generated such that the latitudinal grid spacing is equal to the longitudinal one in each model control volume. This naturally gives the highest resolution in the highest latitudes, where the Rossby radius of deformation is small or even imaginary, thus leading to small-scale slantwise penetrative convection that cannot be well parameterized by popular instant convective adjustment. Debreu and Blayo (2008) reviewed and addressed some important issues in the two-way nesting approaches, including the conservation, inter-grid transfer operators and noise control. Here, we want to emphasize that, with the appropriate choices of numerical operators and grid allocation, additional noise control may not be required due to the minimal errors.

The model strategically uses a blend of Arakawa 'A' (collocated) grid and 'C' (staggered) grid variables. With each control volume, Arakawa 'A' grid is used for the general variables, such as the physical quantity u, v or q (pressure, salinity or potential temperature). The physical quantity is collocated with the velocity components (u, v). The Coriolis terms are also evaluated on the collocated grid and thus have no spatial interpolation error. However, normal face velocity U and V are also staggered at the 'C' grid to impose the mass and energy conservation (Zang et al., 1994). Since the numerical schemes for the pressure equation are written in flux form, the conservation is guaranteed. The current conservative two-way coupling with variable grid sizes is mainly based on this framework. Fig. 2a shows the general overlapping between the coarse and fine grids. Given the DUPOM as an example, the main time integration starts from the eastern domain (NPB domain), whose western boundary matches the eastern boundary of the western domain (TAI domain) with different grid sizes, and adjusts the western boundary inflow to match its net Evaporation–Precipitation (E–P). The same integration is followed for the western domain, and its eastern boundary is adjusted to match its net E–P and the net eastern inflow (latitudinal boundaries are assumed closed).

The grid coupling algorithm uses linear interpolation and the common time filtering technique to ensure simplicity, flux conservation and stability. Their relative locations are shown in Fig. 2. More precisely, they are arranged so that the grid size of the NPB domain is twice as large as that of the TAI domain in a control volume (or finite volume) framework. Each domain uses a boundary ghost zone at cell index $I = 1$, I0 and $J = 1$, $J0$. Note that each domain has its own $I0$ and $J0$. The last longitudinal index ($I = I0$) of the TAI domain is collocated with (actually belongs to) the third longitudinal index ($I = 3$) of the NPB domain (see the schematic). The particular latitudinal grid ($J = 127$) of the NPB domain corresponds to the southernmost boundary of the TAI domain and extends between the second and third latitudinal indices ($J = 2$ and 3) of the TAI domain. The boundary faces of the TAI are located exactly at the center of the NPB cells.[2] The same strategy can be easily extended to multiple domains (Dietrich et al., 2008).

[1] http://www.ngdc.noaa.gov/mgg/global/relief/ETOPO2/.

[2] This grid setting is ideal for the most adequate coupling, but due to the numerical consistency, some variables must be modified for different grid arrangements.

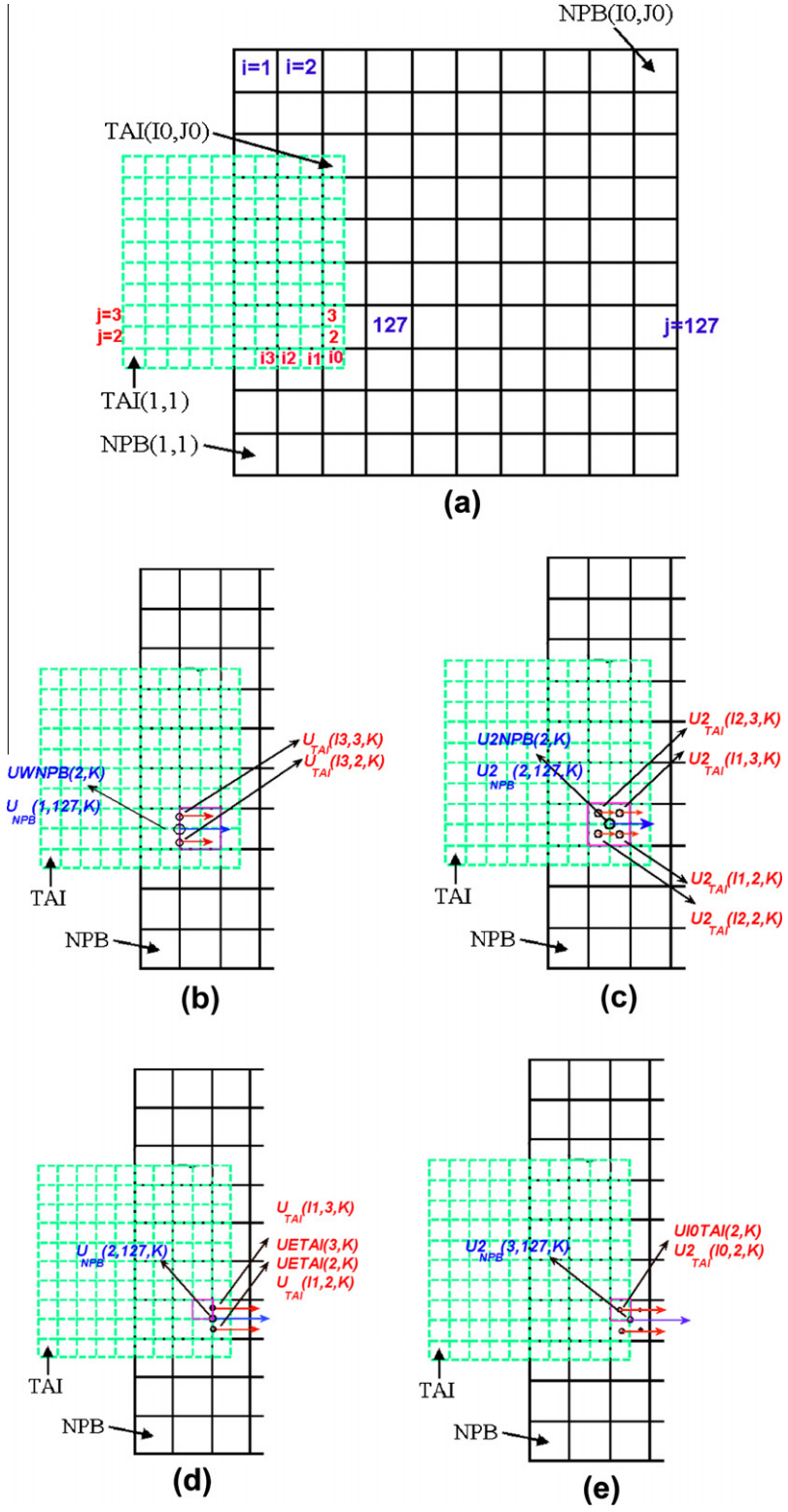

Fig. 2. The schematics of domains and their coupling. (a) The arrangement of TAI and NPB domains. Note that only parts of the grids are shown. The schematics of boundary data exchange from TAI domain to NPB domain: (b) obtain the C-grid variables (*UWNPB* and U_{NPB}); (c) obtain the A-grid variables (*U2NPB* and $U2_{NPB}$). The schematics of boundary data exchange from NPB domain to TAI domain: (d) obtain the C-grid variables (*UETAI* and U_{TAI}); (e) obtain the A-grid variables (*UI0TAI* and $U2_{TAI}$).

2.3.1. Boundary condition of the NPB domain (TAI to NPB)

In finer-to-coarser domain coupling, we transfer fine grid data (TAI) to the first interior zone as well as to the ghost zone of the coarse domain (NPB). Both cell face and cell center boundary conditions are required to ensure the momentum and energy conservation everywhere. Let us define *UWNPB* and $U_{NPB}(1, 127, K)$ (blue arrow) as the intermediate and final cell face velocity U at west interface for the boundary cell (purple square) in the NPB domain (Fig. 2b), respectively. $J = 127$ in the NPB domain corresponds to the southernmost location in the TAI domain. U_{TAI} (red arrow) is

the cell face velocity U of the TAI domain. Hence, $UWNPB$ is directly obtained by the average of the two collocated face velocities U in the TAI domain:

$$UWNPB(2,K) = 1/2 \times (U_{TAI}(I3,2,K) + U_{TAI}(I3,3,K)), \quad (8)$$

where $I3$($I0$–3) is the westward third index cell from the boundary cell ($I0$) of the TAI domain (see Fig. 2b for the location of these variables). Subsequently, U_{NPB}(1, 127, K), the first boundary face velocity in the NPB domain corresponding to the southeasternmost grid in the TAI domain, is obtained using:

$$U_{NPB}(1127,K) = [FLT1 \times UWNPB(2,K) + FLT2 \times (U_{NPB}(1127,K)], \quad (9)$$

where $FLT1$/$FLT2$ are the time filter and $FLT1 = FLT2 - 1$. Since the TAI domain is finer and uses a smaller time step, its associated "frequency" is also smaller. This time filter is applied to avoid numerical stability as a result of time step difference between domains. Note that the land mask array is also applied here to ensure U_{NPB} is zero for the land cells.

At the cell center, $U2NPB$ and $U2_{NPB}$ (blue arrow) are the intermediate and final cell center velocity in the NPB grid (Fig. 2c), respectively. $U2_{TAI}$ (red arrow) is the cell center velocity U in the TAI domain. Since the boundary cell in the NPB domain collocates with four individual cells in the TAI domain, the intermediate velocity $U2NPB$ is obtained by:

$$U2NPB(2,K) = 1/4 \times (U2_{TAI}(I2,2,K) + U2_{TAI}(I2,3,K) + U2_{TAI}(I1,2,K) + U2_{TAI}(I1,3,K)), \quad (10)$$

where $I1$($I0$–1) and $I2$ ($I0$–2) are the westward first and second indices cells from the boundary cell ($I0$), respectively. Similarly, this cell averaging is also applied to other A-grid variables. Subsequently, the updated boundary velocity $U2_{NPB}$(2, 127, K) is obtained using:

$$U2_{NPB}(2127,K) = U2_{NPB}(2127,K) + dU, \quad (11)$$

where dU represents a small incremental difference between the interpolated value from the TAI grid and the cell center value of the NPB grid, $dU = U2NPB(2, K) - U1_{NPB}(2, 127, K)$, at the previous Leap-frog time step. Note that, in order to improve stability, only the increment is added, which can provide a smoother increment. Similar updates are applied to other A-grid variables at $I = 2$.

2.3.2. Boundary condition of the TAI domain (NPB to TAI)

In the western TAI domain, $UETAI$ and $U_{TAI}(I1, 2, K)$ (red arrow) are the intermediate and final cell face velocity U at the east interface for the boundary cell (purple square), respectively. U_{NPB} (blue arrow) is the boundary face velocity U in the NPB domain (Fig. 2d). Since the grid size of the NPB is twice as large as that of the TAI domain, the same grid in the NPB extends latitudinally between the second and third latitudinal indices. Hence, $UETAI$ is obtained directly:

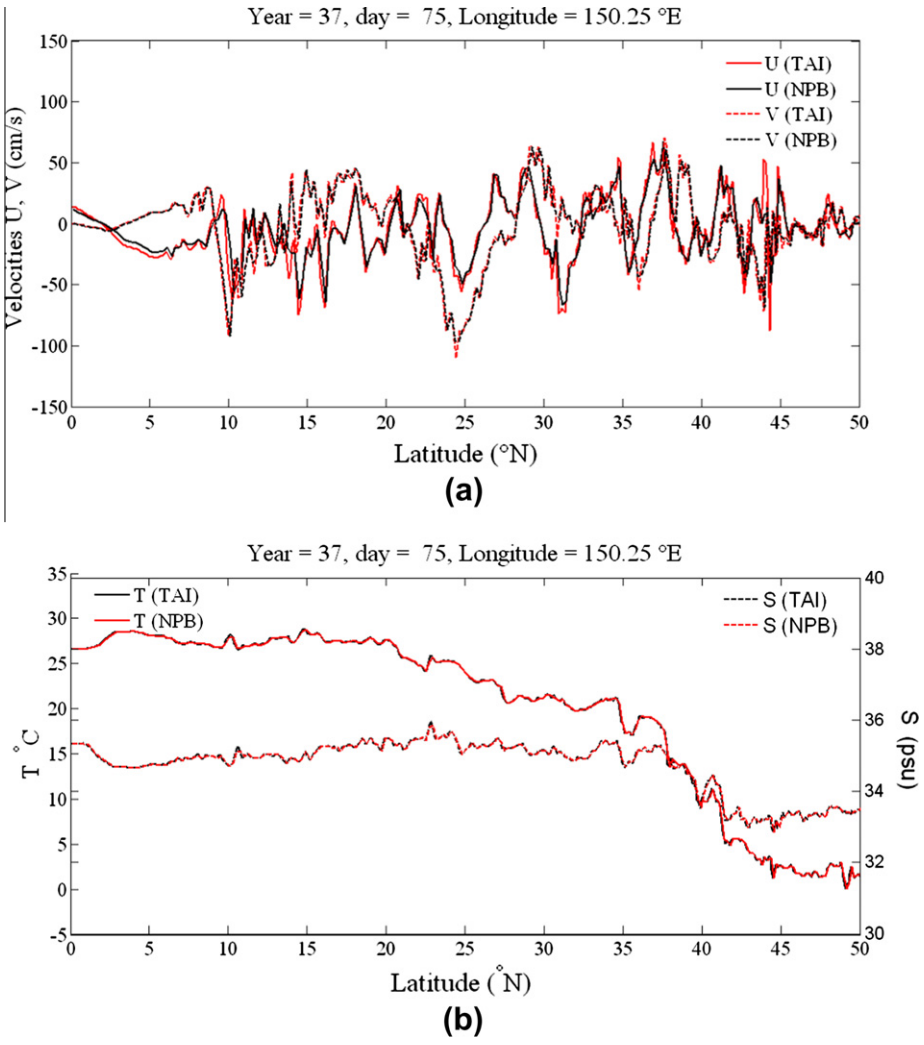

Fig. 3. Comparison of the surface (a) velocities and (b) temperature/salinity along the interface of TAI and NPB domains.

$$UETAI(2,K) = U_{NPB}(2127,K). \quad (12)$$

Similarly, $UETAI(3,K) = U_{NPB}(2,127,K)$. Note that this is the reverse of Eq. (8) and is consistent. Finally, the actual face velocity $U_{TAI}(I1, 2, K)$ is essentially the same as *UETAI* but the land masks are imposed to ensure conservation. This is similar to Eq. (9) without time filter, since the TAI domain uses a finer grid and smaller time step.

The intermediate and final cell center velocity at the boundary in the TAI domain are represented by *UI0TAI* and $U2_{TAI}$ (red arrow), respectively. Since the control volume of the four cell center values (2 hollow + 2 filled circles) of the TAI domain is equivalent to the control volume represented by $U2_{NPB}(3, 127, K)$ which is the cell center velocity *U* (blue arrow) in the NPB domain, the boundary velocity *UI0TAI* is obtained by:

$$UI0TAI(2,K) = U2_{NPB}(3127,K). \quad (13)$$

This is equivalent to the reverse of Eq. (10) and leads to the final A-grid boundary velocity:

$$U2_{TAI}(I0,2,K) = UI0TAI(2,K). \quad (14)$$

In this case, no time filter is required due to the smaller time step. This data exchange is also applied to the other A-grid variables for consistency. These procedures complete a very efficient energy-conserved, two-way coupling algorithm. The instantaneous comparison of the surface velocity and other scalars along the interface between the TAI and NPB domains is shown in Fig. 3. It is clear that the resulting domain coupling is nearly seamless, even with low diffusion and viscosity. No inter-grid sponge layers are applied. Due to the difference in topography or restriction in computation resources, it is sometimes more efficient to use two or more domains (grids). This will also increase the flexibility of the model.

3. General description and model validation

The whole North Pacific Ocean is completely simulated in the DUPOM. Although we mainly focus on the KCS, the remote forcing from the eastern domain may be important for the regional study, including the Rossby waves propagating from the central Pacific. The eastern domain uses a coarse resolution which can still provide appropriate representation of the general North Pacific circulation patterns. Fig. 4 shows the yearly averaged, upper 40 m model velocity vector and equivalent sea surface height of the western North Pacific (TAI domain, top panel) and eastern North Pacific (NPB domain, bottom panel). The two major western boundary currents (Kuroshio and Oyashio) of the subtropical and subpolar gyres are clear in the TAI domain (top). More details about the

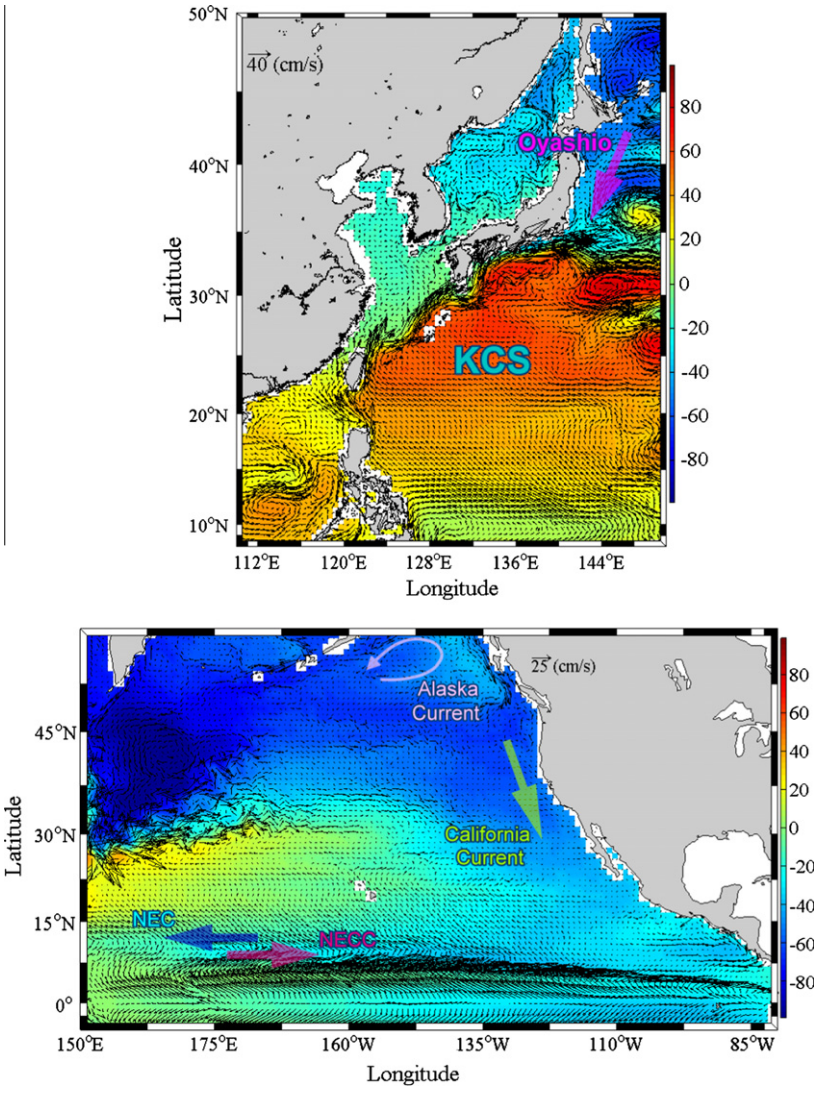

Fig. 4. The yearly averaged model current system of western North Pacific (top panel) and eastern North Pacific (bottom panel). Some key current systems are labeled.

associated features and the KCS will be discussed later. In the NPB domain, the major surface currents are also appropriately resolved. Near the equator, the eastward flowing North Equatorial Countercurrent (NECC) is observed between 0°N and 10°N while the westward flowing NEC has a broader band and locates north of the NECC. In the central Pacific, the KE can extend further eastward before it merges into the North Pacific Current. In the offshore of the Americas, the flow is dominated by the broad, weak (10–30 cm/s) equatorward flowing current, the California Current. The California Current can extend offshore to 900–1000 km and flow year-round. In the Gulf of Alaska, a well-known Alaskan current is also observed in the NPB domain, which flows cyclonically around the Gulf of Alaska, feeding into the Alaskan Stream. All of these surface features are consistent with our understanding of the Pacific current systems.

In this section, we will mainly show some comparison with early observation in the KCS. Fig. 1b focuses on the details in the TAI domain. Several observations are marked and used to validate the current model, including the PCM-1 (east of Taiwan), PN (East China Sea), TK (Tokara Strait), and PCM-5 (ASUKA, south of Japan) lines. The PCM-1 section is located over the Ilan Ridge between the northeast coast of Taiwan and the southernmost island of Japanese Ryukyu at about 24.5°N with a maximum depth of 1000 m. This section is unique because its downstream is the Okinawa Trough (2000 m deep) and its upstream is the western Philippine Sea (depths reaching 5000 m) (Johns et al., 2001; Zhang et al., 2001). It is an ideal location to monitor the transport and variability of the Kuroshio east of Taiwan. Current velocity observations were collected from a current meter array moored along the section at the entrance to the ECS between September 1994 and May 1996 as part of the World Ocean Circulation Experiment. Detailed descriptions can be found in Johns et al. (2001). The PN (Pollution Nagasaki) section is located in the central ECS with a northwest–southeast inclination. Long-term hydrographic observations including quarterly conductivity–temperature–depth (CTD) and shipboard acoustic Doppler current profiler (ADCP) data have been conducted at the PN section by the Nagasaki Marine Observatory of the Japan Meteorological Agency (JMA) since 1972 (Ichikawa and Beardsley, 2002). This section is used to monitor the transport and variability of the Kuroshio in the central ECS (see Kawabe (1988) and Oka and Kawabe (2003) for the details). The TK section is located at the Tokara Strait, which is the main pathway of the

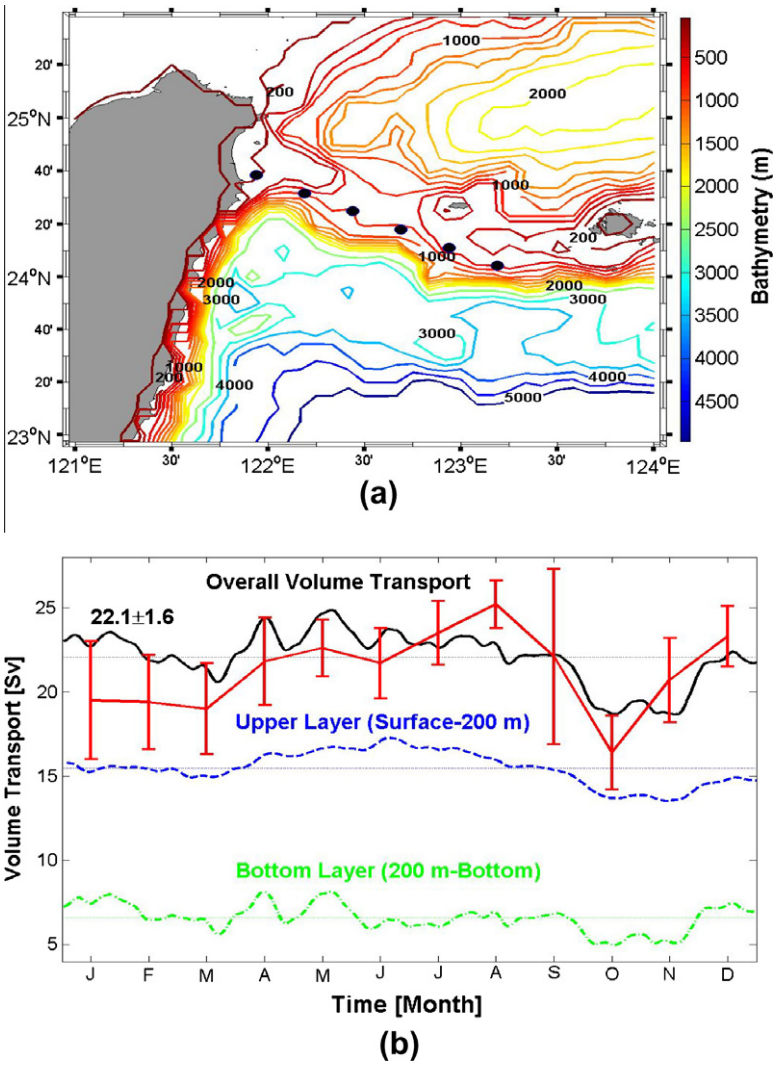

Fig. 5. (a) Major topography of the region east of Taiwan. The PCM-1 line is marked as dots. The contour intervals of the bathymetry are 100 m above 2000 m deep and 500 m below 2000 m deep. (b) Time series of the volume transport across the PCM-1 section during model year 37–39 (5-day running mean, 3-year averaged volume transport within a year). The overall volume transport is shown as the solid line. The dashed and dash-dot lines are the transports above 200 m deep and below 200 m deep, respectively. The red solid line with error bars (the standard deviation in each month) denotes the monthly averaged volume transport of the observation by Taiwan Ocean Research Institute. (For interpretation of the references to color in this figure legend, the reader is referred to the web version of this article.)

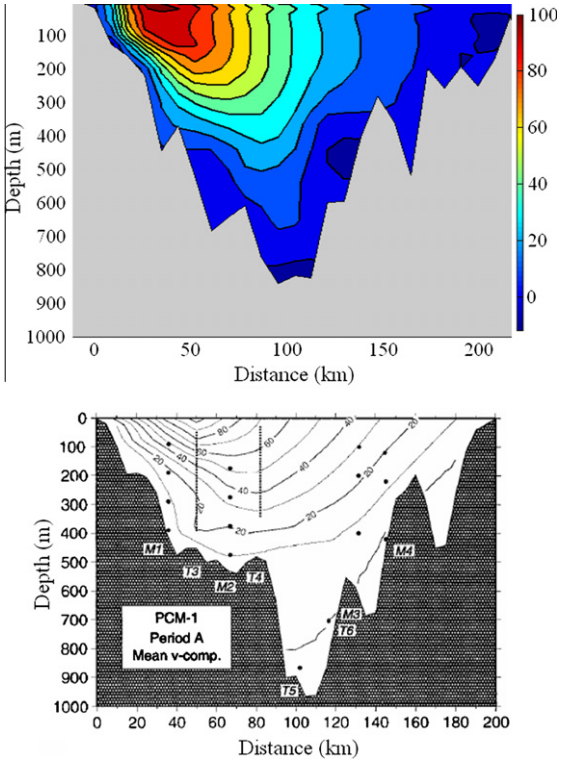

Fig. 6. Comparison of the modeled 3-year mean of the vertical current structure (top) and observation (bottom, Fig. 5 of Johns et al. (2001)) along the PCM-1 section. The contour interval of the velocity distribution is 10 cm/s.

Kuroshio from the ECS to the Pacific south of Japan, near 130°E south of Japanese Kyushu (Feng et al., 2000). Long-term hydrographic data on CTD casts along the TK section has also been gathered seasonally by the JMA Nagasaki Marine Observatory since 1987. The TK line is ideal for monitoring the transport and variability of the Kuroshio south of Kyushu (Kawabe, 1995; Oka and Kawabe, 2003). Finally, the PCM-5 section (also called the ASUKA line) is located south of Japan, extending offshore from the southernmost Cape Ashizuri (Kagimoto and Yamagata, 1997; Yoshinari et al., 2004). The vertical current structures in these sections are compared here to validate the current DUPOM model. Note that these sections are chosen based on the path of the main Kuroshio axis.

3.1. Kuroshio current east of Taiwan

We estimate the volume transport and vertical current structure near the PCM-1, a representative cross-section for the observation of the Kuroshio east of Taiwan (Fig. 5). The total volume transport in Fig. 5a shows a temporal mean of 22.1 Sv and a standard deviation of 1.6 Sv. This indicates the Kuroshio, a strong and northeastward current, constantly flowing through east of Taiwan into the ECS without significant variability. The overall volume transport shows qualitatively similar temporal variations and reasonable agreement with those observed by Taiwan Ocean Research Institute (red solid line shown in Fig. 5b). The slight departure in August and October is not surprising due to the uncertainty. The overall transport is also consistent with the early estimate of a mean transport of 22.6 Sv at the PCM-1 section from repeat CTD/ADCP sections (Liu et al., 1998) and the estimated mean transports of 23.3 Sv with a standard deviation of 2.0 Sv based on the current

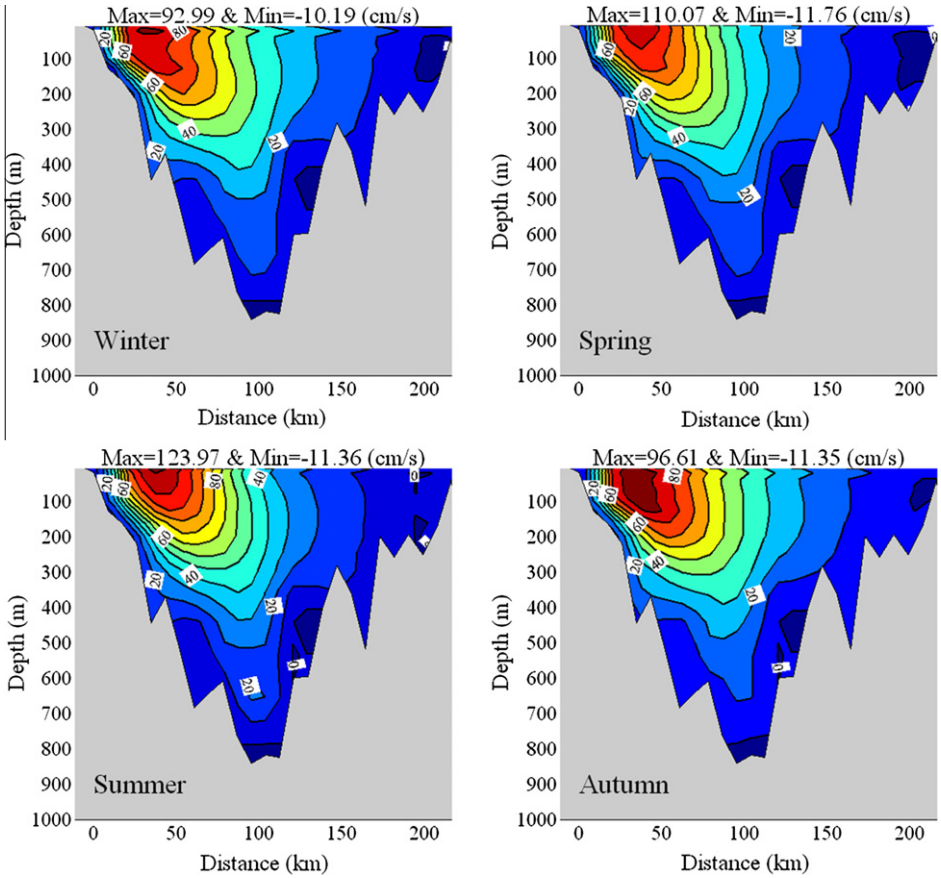

Fig. 7. The seasonal vertical current structure normal to the PCM-1 section during model year 37–39.

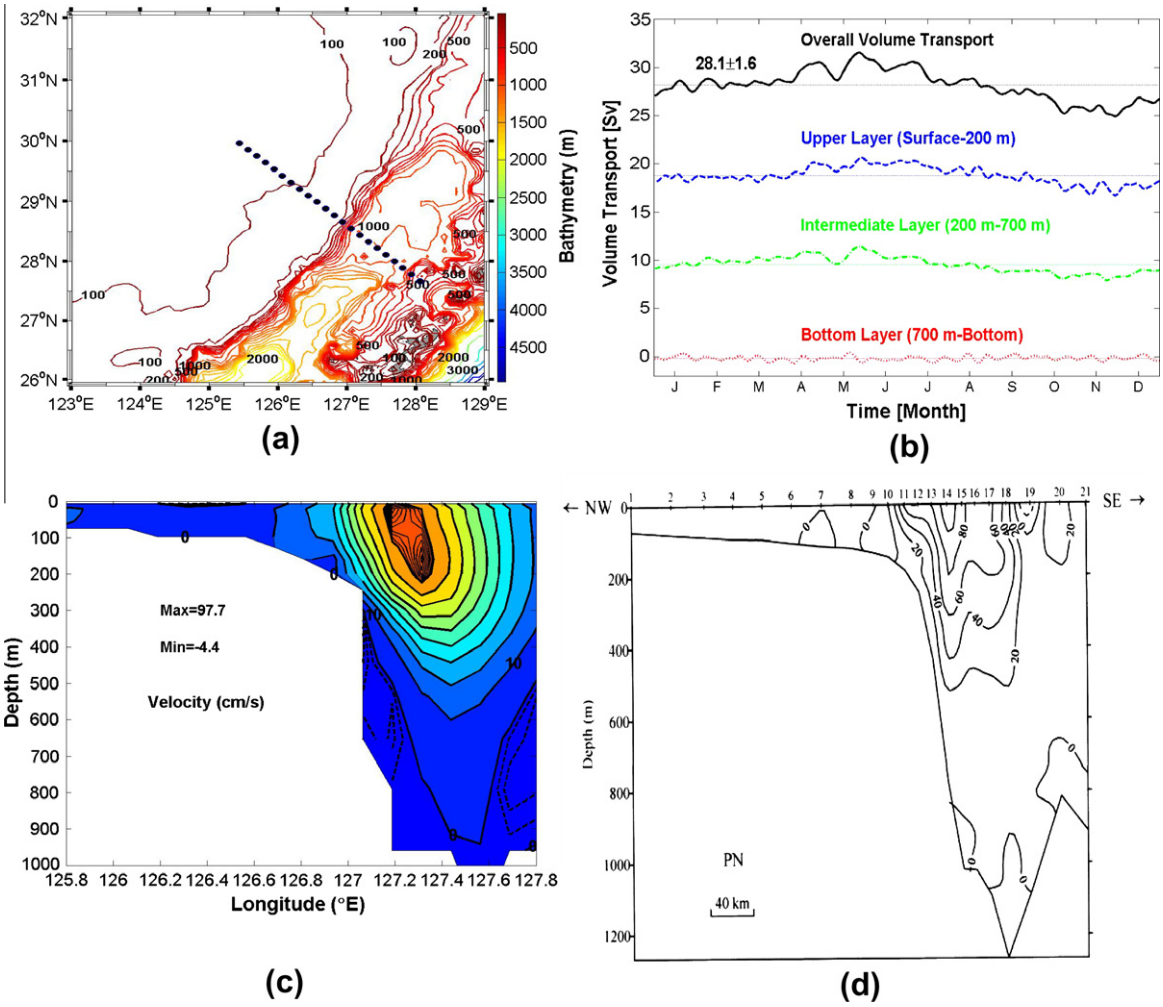

Fig. 8. (a) Major topography of the East China Sea region. The PN line is marked as dots. The contour intervals are the same as that in Fig. 5. (b) Time series of the volume transport across the PN section during model year 37–39. The overall volume transport is shown as the solid line. The dashed, dash-dot, and dotted lines are the transports in the upper layer (surface to 200 m deep), intermediate layer (200 m deep to 700 m deep), and bottom layer (700 m deep to bottom), respectively. (c) Three-year mean of the vertical current structure normal to the PN section. Contour intervals are 10 cm/s within the velocity 0–90 cm/s and 1 cm/s outside the velocity range, respectively. (d) Observation of PN section (Fig. 10 of Yuan et al. (1998)).

meters measurement during September 1994 and May 1996 by WOCE.[3]

The near surface, upper layer current (sea surface to 200 m deep, where the depth of 200 m is chosen since it is close to the continental shelf depth) dominates the volume transport with a temporal mean value of 15.5 ± 1.0 Sv, which accounts for 70% of the overall volume transport. This transport is large in spring and summer (with a maximum of 17.3 Sv), while it is small in autumn and winter (with a minimum of 13.5 Sv), subject to the surface monsoon forcing. The volume transport in the bottom layer (200 m deep to bottom) is always much smaller than in the upper layer. Its temporal mean and standard deviation are 6.6 Sv and 0.8 Sv, respectively, with a larger variance of 12.3% (compared to 6.45% in the upper layer), indicating larger variation at depth. Similar variation of volume transport appears in spring and autumn.

To further study the flow pattern east of Taiwan, we show the 3-year averaged vertical structure at the PCM-1 section during year 37–39 in the top panel of Fig. 6. The strong Kuroshio flows northeastward (positive value), generally at a speed of over 50 cm/s. The current core has a maximum mean velocity of 102.3 cm/s around 40–50 km offshore near 30 m deep. In general, this shows a mean vertical current structure that is similar to the WOCE PCM-1 observation (bottom panel of Fig. 6) for the period from September 1994 to May 1995 (Fig. 5 of Johns et al. (2001)).

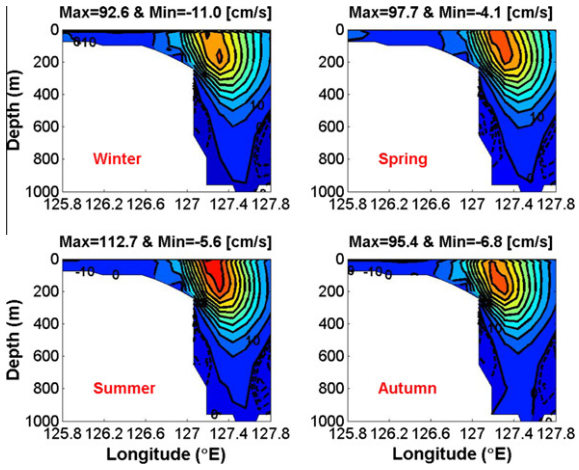

Fig. 9. The seasonal vertical current structure normal to the PN section during model year 37–39.

[3] http://woce.nodc.noaa.gov.

Fig. 7 further shows the seasonal variation of the vertical structure at the PCM-1 section during year 37–39. The vertical structure and the position of the Kuroshio axis do not change significantly, apart from the current core strength as well as the associated downward penetration. This indicates that the Kuroshio axis is potentially controlled by the bottom topography. The seasonal variation of current strength is consistent with the upstream Kuroshio bifurcated from the north coast of Philippine flows (Centurioni et al., 2004). In spring and summer, the upstream Kuroshio flows mostly along the east coast of Taiwan, resulting in larger overall volume transport, as discussed in Fig. 5b. However, in autumn and winter, the main Kuroshio strength east of Taiwan may be

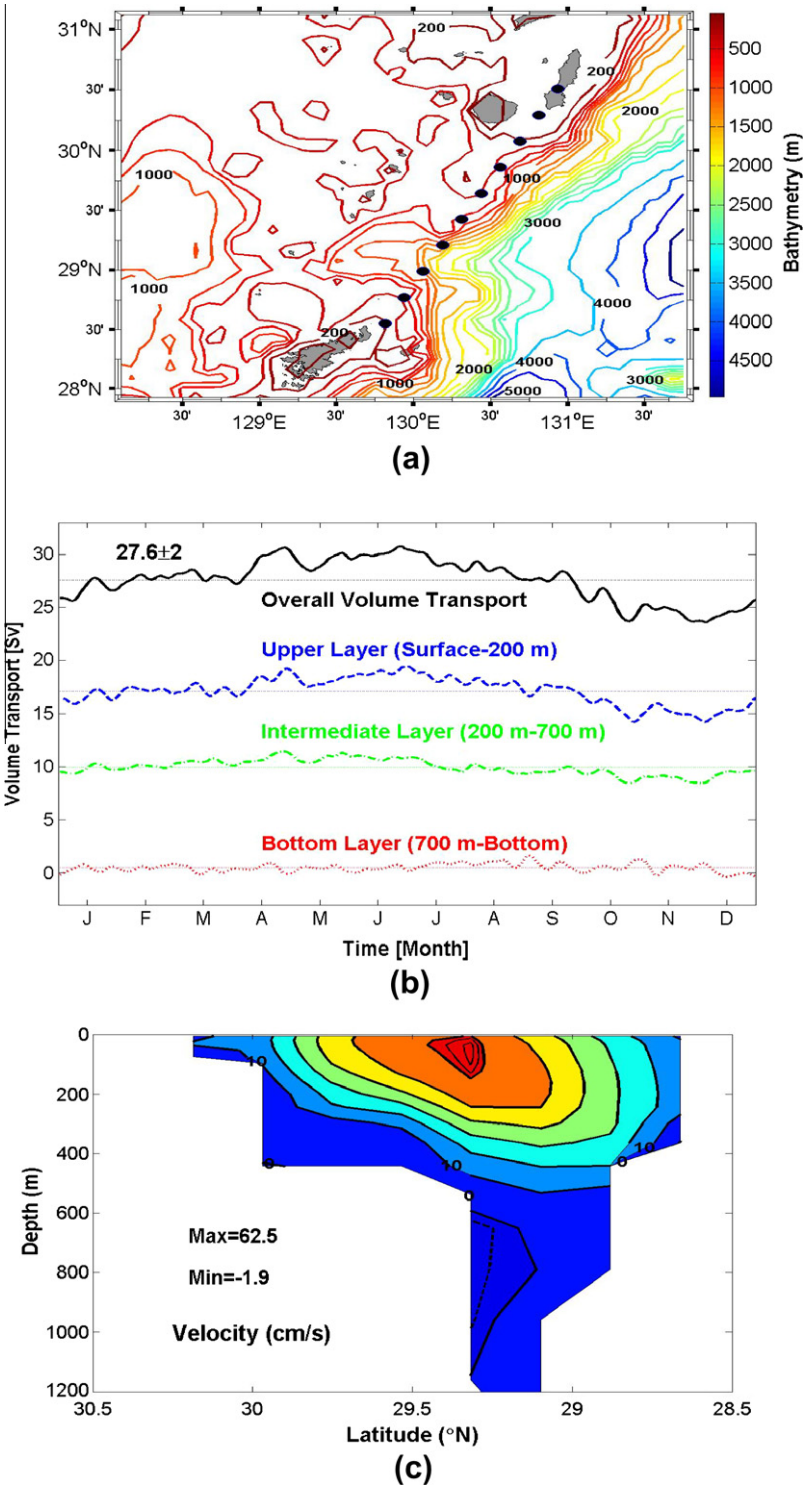

Fig. 10. (a) Major topography of the region south of Kyushu. The TK line is marked as dots. The contour intervals are the same as that in Fig. 5. (b) Time series of the volume transport across the TK section during model year 37–39. The overall volume transport is shown as the solid line. The dashed, dash-dot, and dotted lines are the transports in the upper layer (surface to 200 m deep), intermediate layer (200 m deep to 700 m deep), and bottom layer (700 m deep to bottom), respectively. (c) Three-year mean of the vertical current structure normal to the TK section. The contour intervals are 10 cm/s within the velocity range from 0–60 cm/s and 1 cm/s outside the velocity range, respectively.

weaker due to a larger part of the Kuroshio intrusion into the South China Sea (SCS) through the Luzon Strait (Du et al., 2008). Accordingly, the overall volume transport and current strength are weaker.

3.2. Kuroshio current in the East China Sea

Fig. 8a shows the schematic of the ECS region and the section used to estimate the volume transport and vertical current structure near the PN line, a representative cross-section for the Kuroshio in the central ECS. The bottom topography is constituted by continental shelf and continental slope with a maximum depth of 1000 m. Fig. 8b shows the time series of volume transport flowing across the PN section in a variety of layers during year 37–39 (5-day running mean, 3-year averaged volume transport within a year). The solid line shows the overall volume transport of 28.1 ± 1.6 Sv (northeastward), a few Sv more than that observed in PCM-1. This indicates a stronger northeastward Kuroshio due to the rejoining flow of recirculation gyres near the central ECS. The overall transport agrees reasonably well with the long-term mean geostrophic estimation of 25.4–25.8 Sv referred to 700 db depth across the PN line from 1973 to 1993 (and 2000) (Hinata, 1996; Guo et al., 2002; Ichikawa and Beardsley, 2002). The overall volume transport also reveals clear seasonal variation similar to the variation observed by JMA during winter 1972 to spring 2005, being largest in late spring (31.7 Sv) and smallest in late autumn (24.9 Sv). The upper layer (0–200 m) current dominates the overall transport with a temporal mean of 18.8 ± 0.9 Sv, which accounts for about two-thirds of the overall volume transport. The upper layer transport has a maximum of 20.7 Sv during late spring and a minimum of 16.6 Sv during late autumn. At the deeper layer, the intermediate layer transport (200–700 m deep) contributes about one third of the total transport of 9.5 ± 0.8 Sv, with similar seasonal variation. For the flow in the bottom layer (deeper than 700 m), the volume transport is quite small extending to the bottom topography, which exerts larger drags on the deep current and hence restricts its flow. This leads to a transport of −0.17 ± 0.26 Sv, indicating a rather weak and unstable (southwest) current. Our analysis shows that the strong and northeastward Kuroshio mainly dominates the upper layer transport in the central ECS. A weak and unstable deep countercurrent exists under the Kuroshio.

Similarly, the vertical structure of flow through the ECS is also investigated and compared with the observation. The 3-year averaged vertical current structure normal to the PN section during year 37–39 is shown in Fig. 8c and compares well with the observation data during May–June 1996 in Fig. 8d (Fig. 10 of Yuan et al., 1998). The main Kuroshio (with northeastward velocity more than 50 cm/s) is located between 127°E and 127.5°E just over the continental slope in the upper layer, consistent with the early studies (e.g. Oka and Kawabe, 2003). The detailed current structure shows two distinguishable current cores of different maximum velocities at the sea surface (127.2°E) and subsurface layer of 100–200 m deep (127.3°E), also similar to the observation from December 2002 to November 2004 along the regularly sampled PN-line (Andres et al., 2008). Southwestward current flow also exists under the Kuroshio with a maximum velocity of 4.4 cm/s located at the lateral side of the continental slope. The details and the causes of this countercurrent will be discussed further in a separate paper.

Fig. 9 shows the seasonal variation of the vertical current structure normal to the PN section during year 37–39. Generally, the Kuroshio presents a single current core and exhibits weak seasonal variations in the Kuroshio axis, apart from the appearance of two current cores in winter. The maximum northeastward velocity appears in summer with a value of 112.7 cm/s near the surface. A weak countercurrent exists all year round with the maximum

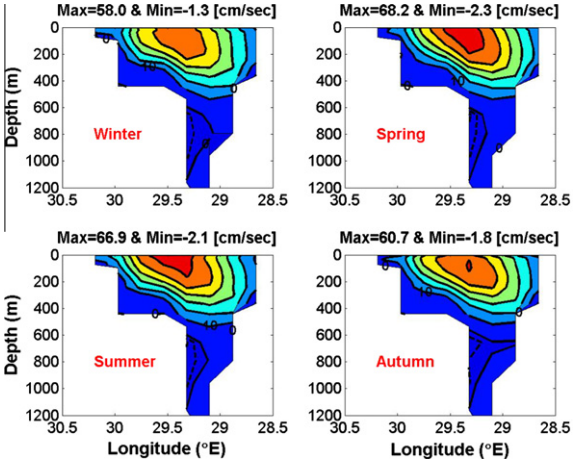

Fig. 11. The seasonal vertical current structure normal to the TK section during model year 37–39.

southwestward velocity of 11 cm/s in winter near the bottom topography. In spring, the Kuroshio core is located around 127.3°E and extends down to subsurface 200 m deep. In summer, the Kuroshio core expands and gets stronger. The maximum speed of the Kuroshio is slightly reduced and the Kuroshio core shifts northwestward and migrates further downward. In winter, the velocity of the Kuroshio is continuously reduced and the single core splits into a pair of current cores with congenial velocity. These structures agree well with the early observation (e.g., Oka and Kawabe, 1998).

3.3. Kuroshio current across the Tokara Strait

Fig. 10a further shows the schematic of the region south of Kyushu near the TK line. The TK line is a northeast–southwest section, representative for the Kuroshio across the Tokara Strait. The bottom bathymetry is characterized by a shallow gap (around 450 m) and a deep gap (1400 m), see Oka and Kawabe (2003). Fig. 10b shows the transport during year 37–39 (5-day running mean, 3-year averaged volume transport within a year). The solid line represents the overall volume transport of 27.6 ± 2 Sv through the Tokara Strait. Note that the southeastward transport is now positive since the Kuroshio here is flowing mostly southeastward. The seasonal variation shows a similar pattern to that observed by the JMA during spring 1987 and spring 2005 with a maximum in spring/summer and a minimum in autumn/winter. The overall volume transport is comparable to the many observations in the past of the Tokara Strait, ranging from 18 Sv to 32 Sv (Bingham and Talley, 1991; Yamamoto et al., 1993, 1998; Feng et al., 2000; Zhu et al., 2006). It is clear that the Kuroshio in the upper layer (<200 m) still dominates the transport with a temporal mean value of 17.1 ± 1.3 Sv, which accounts for over 60% of the overall transport. The transport in this layer has a maximum of 19.5 Sv in summer and a minimum of 14.1 Sv in autumn. The volume transport in the intermediate layer (200–700 m) contributes about 35% of the overall volume transport (9.95 ± 0.73 Sv). Both upper and intermediate layers show similar variation and are consistent with the upstream condition in the ECS. For the bottom layer flow (>700 m), the transport is weak (0.50 ± 0.42 Sv) and fluctuates between southeastwardly (mostly) and northwestwardly (sometimes).

Again, the 3-year averaged vertical current structure normal to the TK section during year 37–39 is shown in Fig. 10c. The strong southeast Kuroshio (>50 cm/s) is located between 29.1°N and 29.7°N. The 3-year averaged vertical current structure is similar to the Type 3 pattern in Oka and Kawabe (2003), i.e., a single south-

ern core with maximum velocity of 62.5 cm/s appears at around 29.3°N. Northwestward current flow exists at the left lateral side of the gap under the Kuroshio.

Fig. 11 shows the seasonal variation of vertical current structure normal to the TK section during year 37–39. It exhibits weak seasonal variations in terms of the position and depth of the Kuroshio axis. The maximum southeastward velocity appears in spring with a value of 68.2 cm/s near the surface. In spring, the Kuroshio core is located at 29.3–29.5°N and extends down to 250 m. The maximum velocity of the Kuroshio starts to decrease after summer. The current core shrinks slightly. The Kuroshio core shrinks significantly in autumn and winter to nearly 100 m deep and shifts southwest-

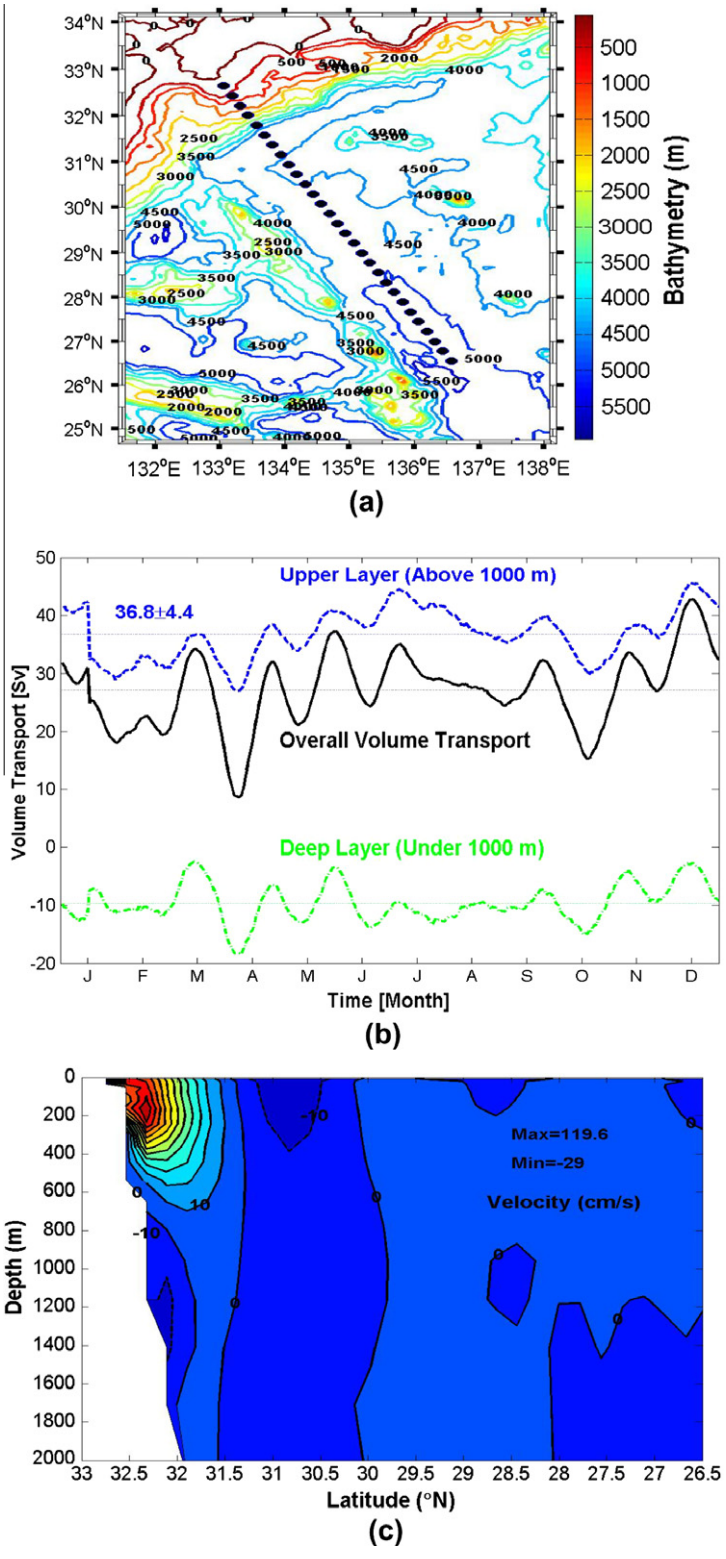

Fig. 12. (a) Major topography of the region south of Japan. The PCM-5 line is marked as dots. The contour interval is 500 m. (b) Time series of the volume transport across the PCM-5 section. The overall volume transport is shown as the solid line. The dashed and green dash-dot lines are the transports in the upper (above 1000 m deep) and deep (under 1000 m deep) layers, respectively. (c) Three-year mean of the vertical current structure normal to the PCM-5 section. The contour intervals are 10 cm/s.

ward. Furthermore, an undercurrent extends from left of the gap to right in autumn and winter, while it appears at the left side of the gap in spring and summer.

In general, very similar temporal variations are observed along the PCM-1, PN, and TK sections. The overall transports in these three sections are larger in spring and summer. The main Kuroshio core is confined in the upper layer. Undercurrents can be observed in all these sections along the continental slope. The temporal mean of the overall volume transport across the PN section (28.1 Sv) is larger than that across the PCM-1 section (22.1 Sv), indicating enhanced flow entering the ECS rejoining the Kuroshio (partly from the Taiwan Strait and recirculation). The temporal mean of the overall volume transport across the TK section (27.6 Sv) follows the trend across the PN section, indicating that most of the Kuroshio water in the ECS flows into the Tokara Strait, while a branch of the Kuroshio flows into the Japan/East Sea through the Tsushima Strait (Fig. 1c).

3.4. Kuroshio current south of Japan

The Kuroshio south of Japan varies more significantly than at the upstream. Fig. 12a shows the schematic of the region south of Japan and the locations of the PCM-5 line. The PCM-5 section extends from the southernmost cape of Japanese Shikoku, Cape Ashizuri, to the offshore Pacific and forms a northwest–southeast line. The bottom topography along the PCM-5 is very shallow nearshore and drops rapidly to a maximum depth of 5000 m offshore (Kagimoto and Yamagata, 1997; Kashima et al., 2003). Fig. 12b shows the volume transport during year 37–39 in the upper (<1000 m) and bottom (>1000 m) layer (5-day running mean, 3-year averaged volume transport within a year). The dashed line shows the upper layer transport of 36.8 ± 4.4 Sv, which includes the nearshore northeastward Kuroshio and offshore recirculation. However, a large amount of fluctuation is observed from 27.0 Sv (spring) to 45.7 Sv (summer and winter), showing significant variability. The large variation in the PCM-5 transport suggests a cause of the intensification of the Kuroshio recirculation and instability. The inter-annual variability is also quite clear from the model results (not shown here), although the climatological forcing is imposed. This indicates strong eddy activities in this area and relates to the dynamic of meander paths. Since the intensive eddies intrude into the Kuroshio recirculation region and circulation in this region, the transport across the PCM-5 (ASUKA) line varies vigorously. In general, the upper layer transport agrees reasonably well with

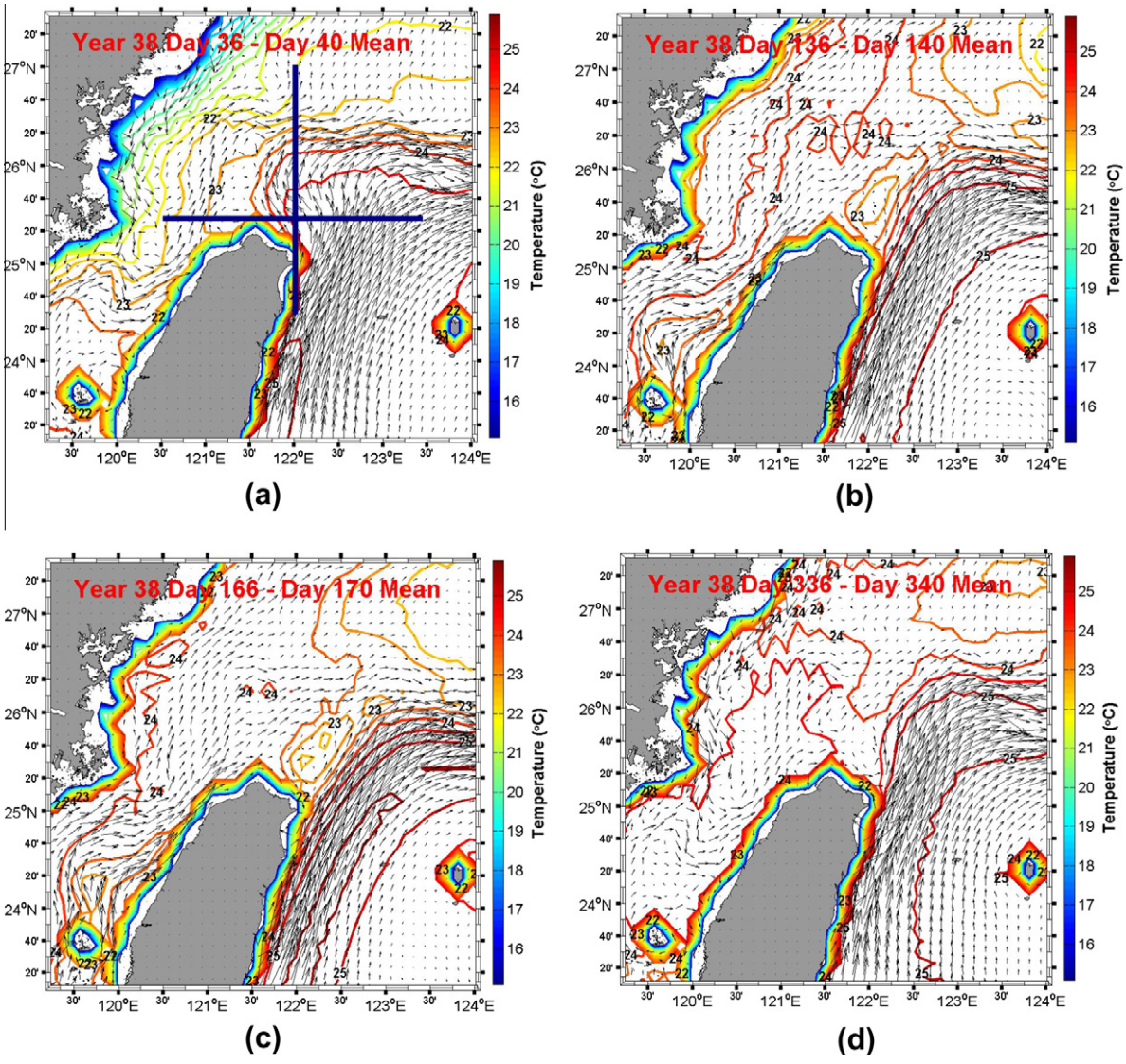

Fig. 13. Distribution of 5-day averaged temperature and horizontal velocity at depth of 20 m north of Taiwan in year 38. The contour interval of the temperature is 0.5 °C: (a) day 36–40, (b) day 136–140, (c) day 166–170, and (d) day 336–340. The blue lines show the vertical section lines of 122°E and 25.5°N in Figs. 14 and 15, respectively. (For interpretation of the references to color in this figure legend, the reader is referred to the web version of this article.)

the earlier studies but with slightly smaller transport (Kagimoto and Yamagata, 1997; Imawaki et al., 2001; Yoshinari et al., 2004). This is mainly due to the deep countercurrent observed in the model results. The green dash-dot line shows the negative bottom layer transport below 1000 m, indicating a stable and southwestward countercurrent. Hence, the total transport across the PCM-5 is always northeastward but smaller.

We further investigate the vertical structure. The 3-year averaged vertical structure normal to the PCM-5 section during year 37–39 shows a pair of opposite current cores down to the subsurface layer (Fig. 12c). The core of Kuroshio, defined as the mean velocity >50 cm/s, is located between 32°N and 32.5°N near the south coast of Japan with the maximum around 200 m. The offshore southwestward Kuroshio recirculation is broad and has a maximum velocity of 19.4 cm/s near the surface. An undercurrent core with a depth of 1100–1500 m is also observed beneath the Kuroshio near the bottom topography. In addition, two countercurrent cores of the Kuroshio recirculation can be seen offshore of the south coast of Japan. These characteristics are consistent with those reported earlier (Kagimoto and Yamagata, 1997).

4. Cold dome northeast of Taiwan

The high resolution DUPOM is useful to further diagnose the coastal dynamics in the Asian Marginal Seas while maintaining computational efficiency. The remote forcing (e.g. Kuroshio) is well-resolved rather than specifying. Here, we discuss the appearance of the cold dome northeast of Taiwan.

Fig. 13 shows a few representative 5-day averaged temperature and velocity fields at a depth of 20 m north of Taiwan. The temperature distribution north of Taiwan in late winter (Fig. 13a) is generally less than 25 °C and decreases towards the continental shelf in ECS (from 24.5 °C to 22.5 °C). The Kuroshio core is located much closer to east of Taiwan so that the cold dome is not easy to observe. Note that there exists a southward China Coastal Current (CCC, commonly found in winter) flowing equatorward along the China coast, and its branches also flow into the north coast of Taiwan. The existence of the CCC seems to reduce the northward transport through the TS and may affect the intrusion of the Kuroshio to northeast Taiwan. These regional flow patterns are mainly dominated by the winter monsoon forcing in the model. Fig. 13b shows another scenario around Taiwan in late spring. The CCC disappears with enhanced TS transport (Jan et al., 2002), which may force more TS throughflows to flow over the north coast of Taiwan in association with further offshore Kuroshio. Thus, a cold dome with low temperature (<23 °C) and cyclonic circulation is easily observed northeast of Taiwan. The TS through flow seems to influence the Kuroshio core variation northeast of Taiwan, similar to the island wake formation behind the island. This cyclonic circulation can also enhance the potential upwelling of subsurface water. Fig. 13c shows two weak centers of the cold dome with tempera-

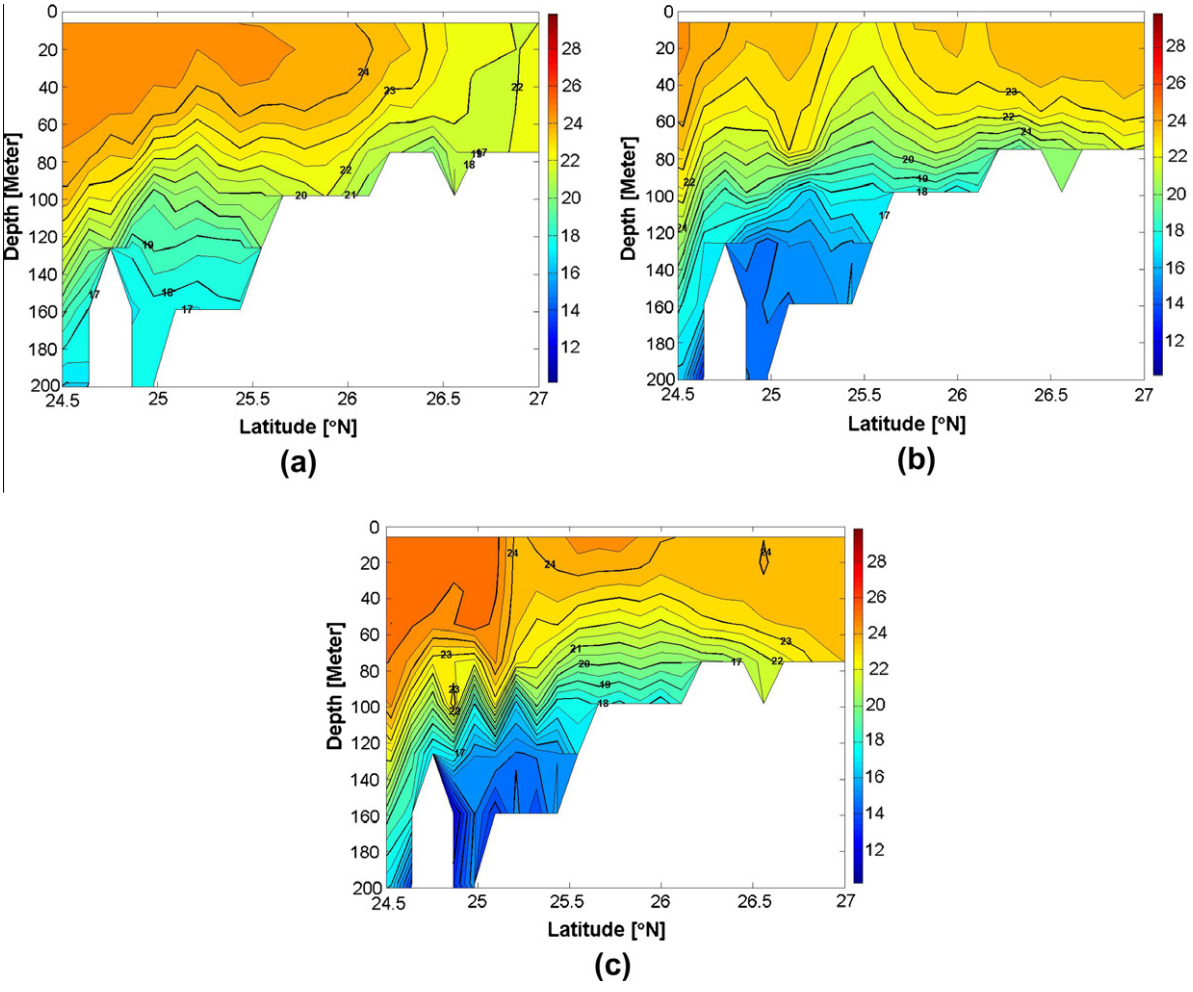

Fig. 14. Contour of 5-day averaged temperature along 122°E in year 38. The contour interval of the temperature is 0.5 °C: (a) day 36–40, (b) day 136–140, and (c) day 336–340.

ture less than 22.5 °C northeast of Taiwan in summer. Consistent with the observation, the cold dome in the model is frequently formed in summer rather than other seasons. The strengthening of the CCC with weakening TS throughflow in early winter is also associated with the disappearance of the cold dome (Fig. 13d). These characteristics are also observed in the earlier literatures (Tang et al., 2000).

Figs. 14 and 15 show the corresponding 5-day averaged vertical temperature sections along the typical cold dome center (122°E and 25.5°N, respectively). When no cold dome is observed, as shown in Figs. 14a and 15a, the temperature distribution and stratification follow the topography accordingly with decreasing temperature shoreward. The warm Kuroshio core moves inshore and contributes significantly to the deeper mixed layer of high temperature. When the cold dome is formed (Figs. 14b and 15b), the surface mixed layer is quite uniform, except a local minimum is formed around 25.5°N and 122.2°E. The results show that the cold dome formation may be associated with strong local upwelling and the remote Kuroshio. The cold water results mostly from the subsurface Kuroshio water and can maintain up to 2–3 °C horizontal gradient in strength. The strong local upwelling enhances the pumping of cold water, which comes from the cyclonic eddy due to the offshore Kuroshio variation (Tang et al., 2000; Wu et al., 2006). The typical size can extend up to 30–50 km wide in diameter and penetrate down to 60–80 m depth. Panels (c) of Figs. 14 and 15 show the relaxation of upwelling and the restratification of the surface mixed layer. The cold-dome formation is closely related to the Kuroshio path in the ECS and its sub-mesoscale dynamics. The transport of the TS outflow and the CCC also modulate its formation and the subsurface upwelled water. The cold dome formation in summer is usually associated with the frequent passage of typhoons through the air–sea interaction and lasts for a few days (Shen et al., 2011). These interactions also complicate the regional flow patterns northeast of Taiwan.

5. Variability of the Kuroshio meanders

The variation of the Kuroshio meanders southeast of Japan is of great interest due to its large influence on fisheries, ship navigation, climate feedbacks and others. However, the generation mechanisms of its variation and interaction with deep current system are still unclear. Many early studies attributed the path variability to the upstream velocity and volume transport of the Kuroshio in Tokara Strait (e.g., Kawabe, 1985). A number of numerical studies have been carried out to reproduce the Kuroshio path variation using inflow–outflow regional models and basin-scale high resolution models (Endoh and Hibiya, 2000; Masuda and Akitomo, 2000; Masuda et al., 1999). These numerical experiments prescribed the short-term variation of the Kuroshio current velocity in the Tokara Strait. It is unclear if the short-term velocity variation in the Tokara Strait was the main cause. The transport in Tokara Strait during the LM path is usually larger than that during the NLM path (e.g., Kawabe, 1980; Saiki, 1982). However, larger upstream velocity cannot guarantee the occurrence of the LM. Hurlburt et al. (1996) found that the stratification and wind stress could change the frequency of the LM path through baroclinic instability west of the Izu Ridge. Recent studies suggested the formation of the Kuroshio LM in 2004 resulted from the generation of a large-amplitude trigger meander southeast of Kyushu and a cyclonic eddy on the offshore side of the Kuroshio. Several numerical experiments have been performed to examine how an anticylonic eddy in ocean models triggers the path transition from the nNLM path to the oNLM path (Mitsudera et al., 2001; Waseda and Mitsudera, 2002) or to the LM path (En-

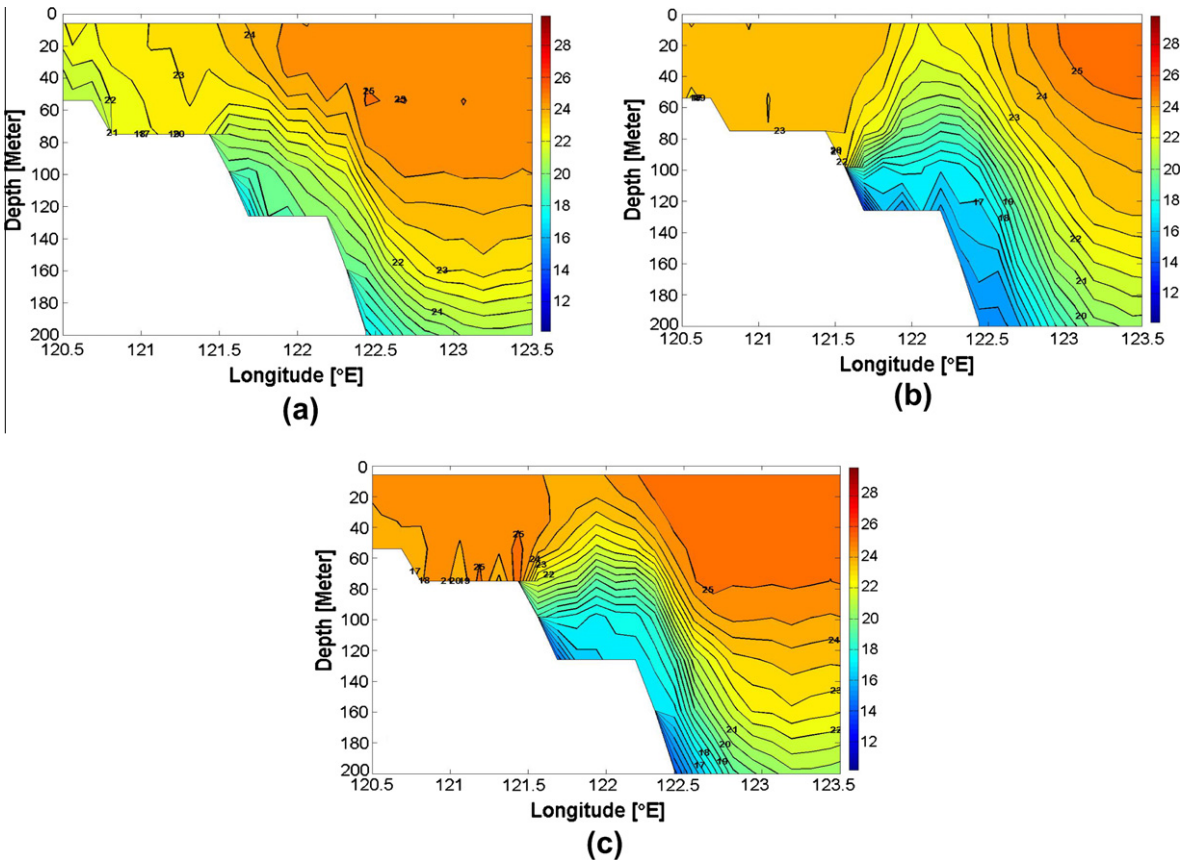

Fig. 15. Same as Fig. 14 except along latitude 25.5°N.

doh and Hibiya, 2000; Akitomo and Kurogi, 2001; Miyazawa et al., 2008; Usui et al., 2008). Waseda and Mitsudera (2002) used a high-resolution ocean general circulation model to simulate the interaction between the observed mesoscale eddy and the Kuroshio. They found that the westward propagating anticyclonic eddy could trigger the short-term Kuroshio meander south of Japan. Particularly, the trigger meander southeast of Kyushu in 2004 was caused by downstream advection of anticyclonic eddies along the Kuroshio in the ECS from east of Taiwan, which brought a high potential vorticity anomaly to generate the small meander (Miyazawa et al., 2008; Usui et al., 2008).

It is very interesting that the DUPOM model dynamically generates different meander paths throughout the years. The time scale for the variation is significantly larger, which confirms the significant inter-annual variability in PCM-5 line diagnostics. Three different types of the Kuroshio path south of Japan can be seen in the model. Fig. 16 shows the snapshot of the sea surface temperature (SST) and surface velocity field for the typical Kuroshio meander patterns. An nNLM is shown in Fig. 16a, where the strong Kuroshio flows northward through east of Taiwan, turns northeastward and enters the ECS along the continental slope. The Kuroshio veers and enters the Tokara Strait south of Kyushu at around 30°N. The existence of Kyushu and the Tokara Strait is the primary cause for this turn as the KC flows along the f/H contours. After passing the strait, the Kuroshio veers again and flows northward to reach the southern coast of Japanese Shikoku. Then it flows northeastward along the southern coast of Japan. The mean Kuroshio speed and its spatial variation increase progressively from south of Kyushu to the Izu Ridge. Two westward propagating cyclonic cold eddies appear south of Japan, which are commonly found in the simulation. In Fig. 16b, the Kuroshio path is similar before it enters the Tokara Strait. The Kuroshio veers at a more southerly position of 29.5°N and flows through the Tokara Strait. After leaving the strait, the Kuroshio flows northeastward to reach the Kii Peninsula of Honshu and flows southeastward a little bit. This path can be defined as the transition period between the nNLM and oNLM paths (Kawabe, 1995). Similar transition is also frequently found showing the unsteadiness in this region.

Fig. 16c shows how the Kuroshio takes a southern position of 29.5°N to pass the Tokara Strait and introduces a larger curvature south of Kyushu. The Kuroshio then takes a more easterly position east of 132°E, veers and flows northward to reach the southern

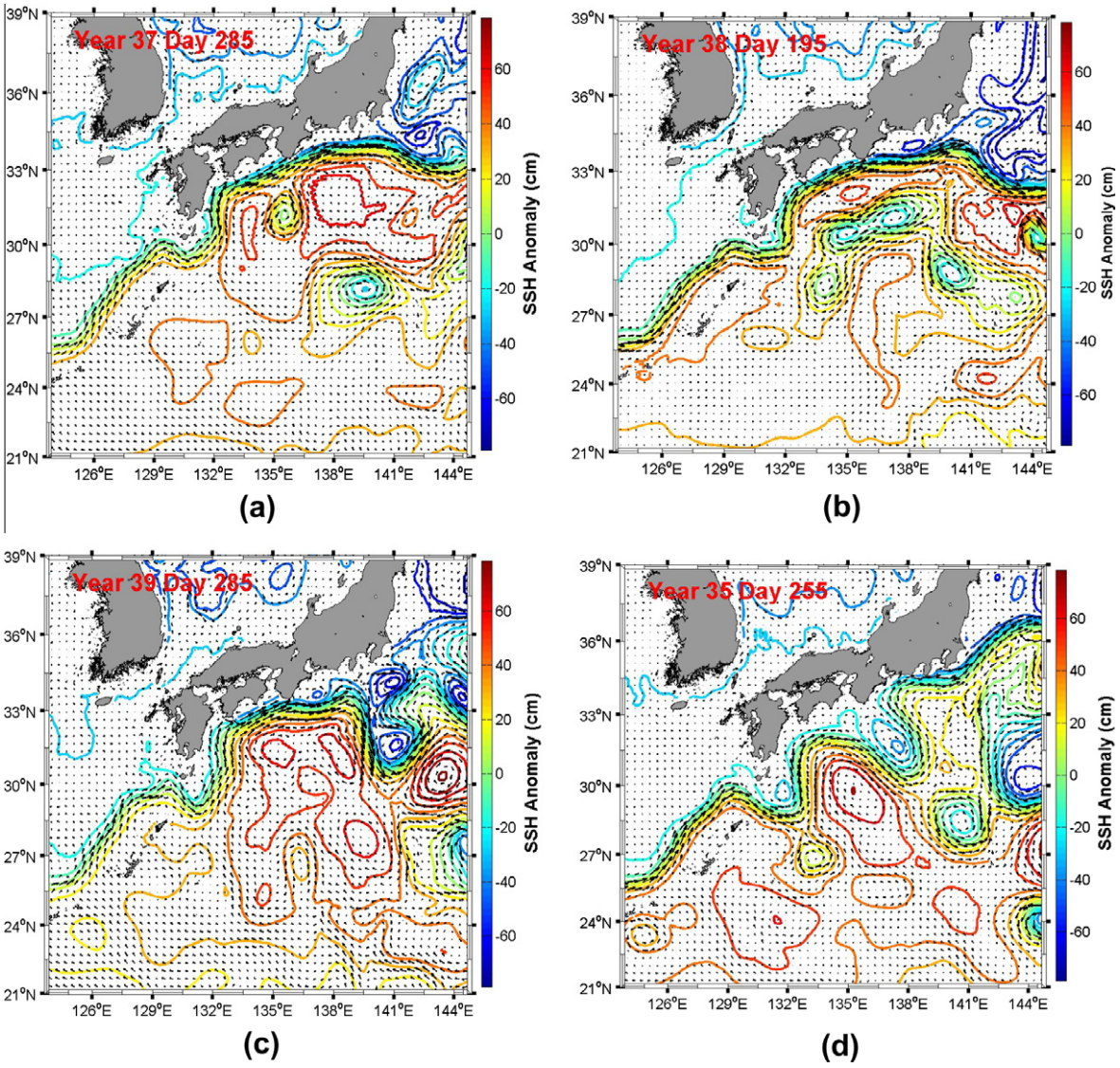

Fig. 16. Snapshots of sea surface elevation anomaly (unit in cm) and surface horizontal velocity: (a) typical nNLM path in year 37 day 285, (b) transition of path variation in year 38 day 195, (c) oNLM path in year 39 day 285, and (d) LM path in year 35 day 195.

coast of Japanese Shikoku. Finally, the Kuroshio flows northeastward along the south coast of Japan and flows away from the south coast of Japan after it reaches the Kii Peninsula of Japanese Honshu. In this case, the Kuroshio takes the so-called oNLM (Kawabe, 1995). Fig. 16d shows a typical Kuroshio LM taken in model year 35. The LM path is characterized by a Large Meander south of Japan around 136°E and the main axis is very close to the southern coast of Shikoku.

Fig. 17 further shows the snapshot of the vertical current structure normal to the TK section located at the Tokara Strait south of Japanese Kyushu, corresponding to Fig. 16a–c, respectively. Fig. 17a shows a pair of current cores with velocity greater than 80 cm/s when the Kuroshio flows through the TK section. One current core is near the surface and is located broadly north of 29.5°N. The other current core is located around 29.3°N in the subsurface layer of 250 m deep. The pattern with both current cores corresponds to the Type 1 and 2 proposed by Oka and Kawabe (2003). The undercurrent exists in the intermediate layer and bottom layer. Fig. 17b shows a single current core when the Kuroshio flows through the TK section. The current with a maximum surface velocity greater than 100 cm/s is located north of 29.7°N. The undercurrent exists at the western lateral side of the gap in the intermediate layer and bottom layer. In Fig. 17c, the current has a maximum velocity of 62.5 cm/s at 200 m. The undercurrent exists both at the western lateral side and the eastern lateral side of the gap from the intermediate layer to the bottom layer. Previous studies indicate that the Kuroshio path variation depends on the flow condition south of Kyushu. From the model results, we cannot find any direct link between the Kuroshio path variability and the upstream velocity and transport in the Tokara Strait.

Fig. 18a shows the modeled location of the Kuroshio axis along 138°E, which is a good indicator of the Kuroshio path type. The position of the Kuroshio axis is defined as the latitude of the maximum surface velocity (Ambe et al., 2004). The time period is from the modeled year 35 to 46. It is clear that a LM path begins to form around the end of year 43 and lasts for more than 2 years. Several oNLM paths are also observed occasionally. However, their existence does not last very long. The model results show strong non-linear dynamics in the Kuroshio path variations and several modes of instability may dominate at different scales. It is found that the LM observed in 2004 is triggered by a small meander southeast of Kyushu, and the Sea Surface Height Anomaly (SSHa) there reaches its local minimum (e.g., Usui et al., 2008; Miyazawa et al., 2008). Fig. 18b shows the time series of the modeled SSHa averaged over southeast of Kyushu (30–33°N and 131–134°E). Note that the modeled LM path is also triggered by a local minimal SSHa. However, the triggering minimal SSHa is not the largest negative SSHa observed in our time series. The largest negative SSHa is found during the period of LM paths and results from a large westward propagating cyclonic eddy which is pinched off from the LM. The cold cyclonic eddy originally lies stationary in the LM path of the Kuroshio southeast of the Kii Peninsula. It was pinched off from the LM and moved westward offshore of the Kuroshio. The pinched-off cyclonic eddy from the LM can be found in Fig. 18a due to the significant variation of the LM path location. Fig. 18c further shows the corresponding SSHa along 138°E in the model year

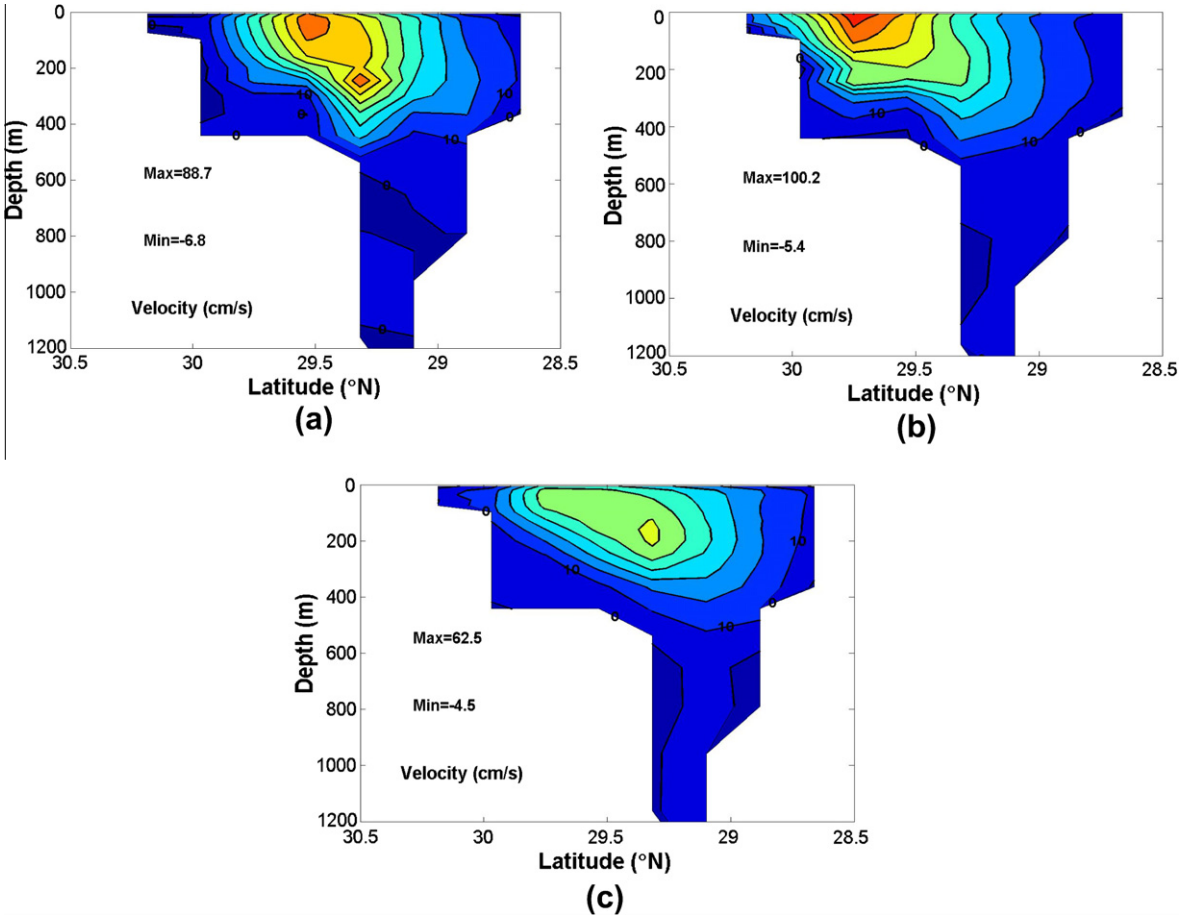

Fig. 17. Snapshot of the vertical current structure normal to the TK section in the Tokara Strait: (a) year 37 day 285, (b) transition of path in year 38 day 195, (c) oNLM path in year 39 day 285.

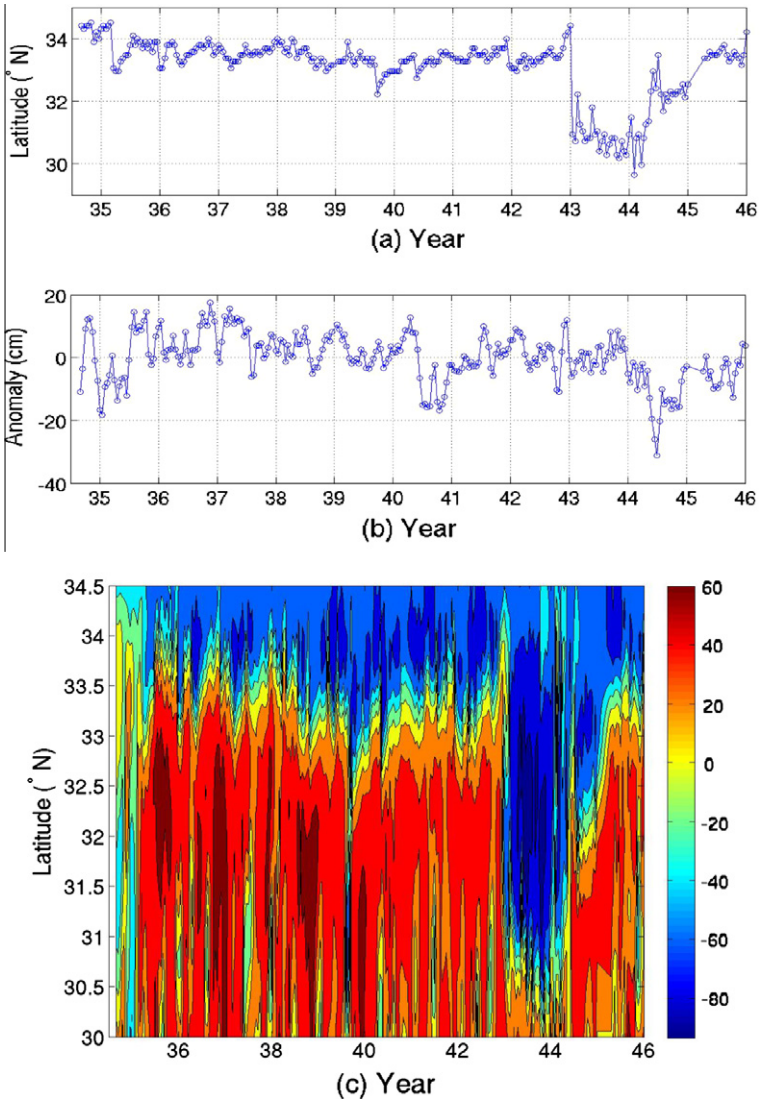

Fig. 18. (a) The modeled location of the Kuroshio axis along 138°E during year 35–46, which is a good indicator of the Kuroshio path type. The position of the Kuroshio axis is defined as the latitude of the maximum surface velocity. (b) The time series of the modeled SSHa averaged over southeast of Kyushu (30–33°N and 131–134°E). (c) The corresponding SSHa v.s. latitude along 138°E in the model year 35–46.

35–46. The variation of meander paths is very clear and shows a long period of LM. The strong variation of SSHa indicates a large regional instability feature. After the pinch-off of the cyclonic eddy, the amplitude of the LM reduces and the SSHa field remains stable for a few months. Then the Kuroshio path moves gradually northward and the amplitude reduces further before the Kuroshio approaches the coast of the Kii Peninsula. This is very similar to the variation of LM in late May 1977 and early April 1979 (Kamihira et al., 1978; Nishida, 1982). However, in our simulation, the cold eddy is no longer reattached to the Kuroshio. A pinched-off eddy rarely occurs south of Japan, although it occurs frequently in the KE east of Japan. The model results also indicate that the nNLM usually corresponds to the high SSHa southeast of Kyushu. Most of the oNLM or LM can be triggered by the low SSHa in the model. However, not all negative SSHa southeast of Kyushu corresponds to the oNLM or LM paths.

The modeled formation process of the LM is detailed in Fig. 19. The LM formation is initialized around the end of modeled year 43. Fig. 19a–h shows the instantaneous surface velocity vector superimposed with the SSHa every 30 days. The variation of the Kuroshio axis position is relatively small from south of Kyushu to off the Shikoku, where the variation is smallest, while the variation is very large around the Izu Ridge. Similar to earlier studies, the horizontal gradient of the Kuroshio speed southeast of Japan is larger at the coastal side of the current axis than the offshore side. A small meander southeast of Kyushu is first generated in Fig. 19a. A small cyclone anomaly is generated between the main Kuroshio path and the Japanese coast. This cyclonic eddy is associated with interaction between the intensive westward propagating cyclonic eddies and the Kuroshio axis. It develops further and forms the small meander southeast of Kyushu. This corresponds to the low SSHa observed in Fig. 18b before the formation of the LM. Another similar cyclonic eddy centered at 137°E along similar latitude is also presented in Fig. 19a. Note that an anti-cyclonic eddy also moves northwestward at 133°E from the central Pacific. The northwestward moving anti-cyclonic warm eddy seems to interact with the Kuroshio southeast of Kyushu and other eddy fields, merging into a larger system southeast of Kyushu. This interaction squeezes the cyclonic eddy to move eastward along the coast, which triggers the subsequent LM and causes the sudden increase of SSHa before the formation of the LM in Fig. 18b. The eastward propagating cyclonic eddy triggers the small meander, which evolves into the LM

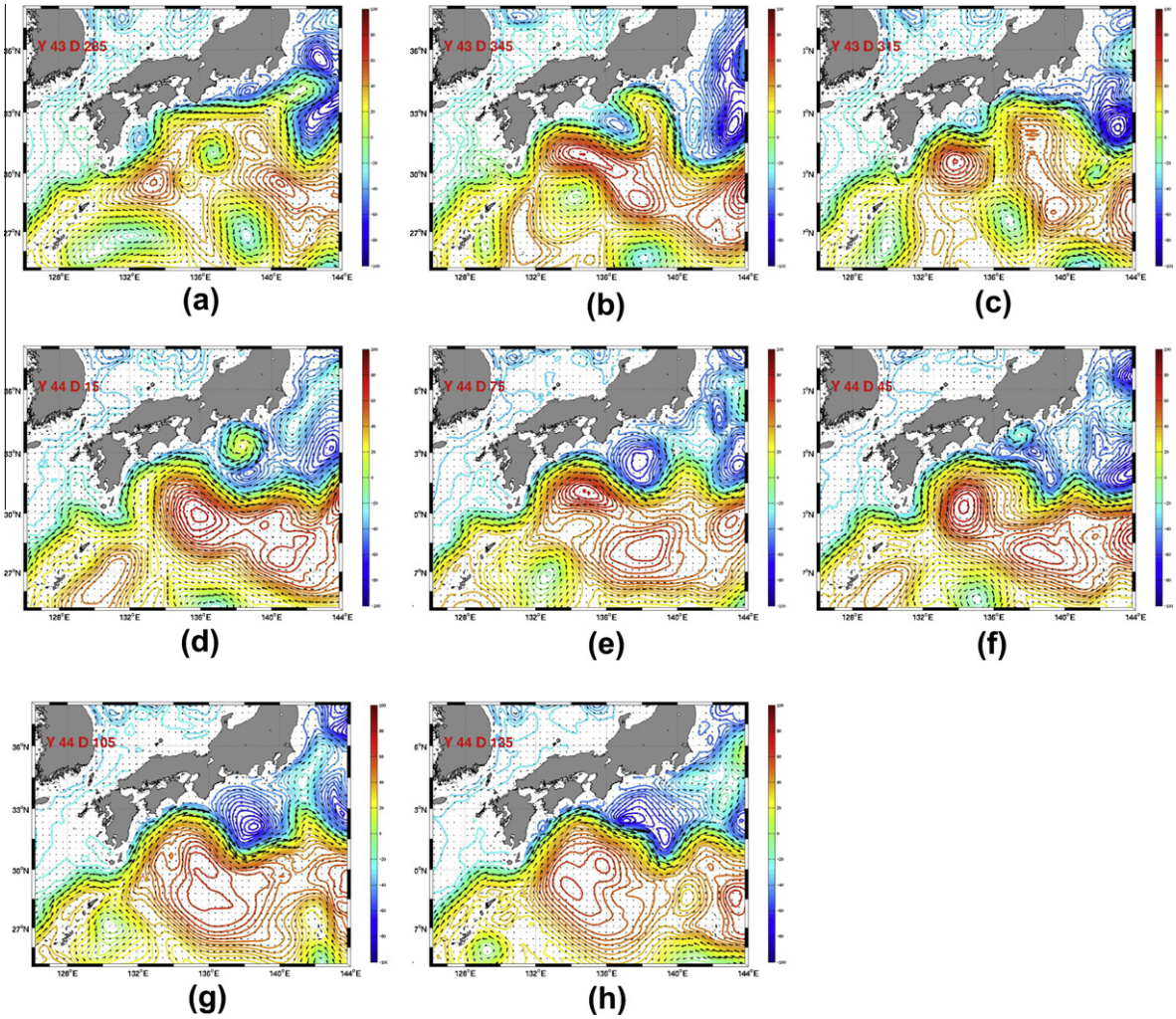

Fig. 19. The instantaneous surface velocity vector superimposed with the SSHa (unit in cm) every 30 day, showing the formation of Large Meander. The time sequence is from left-top (a) to right-bottom (h).

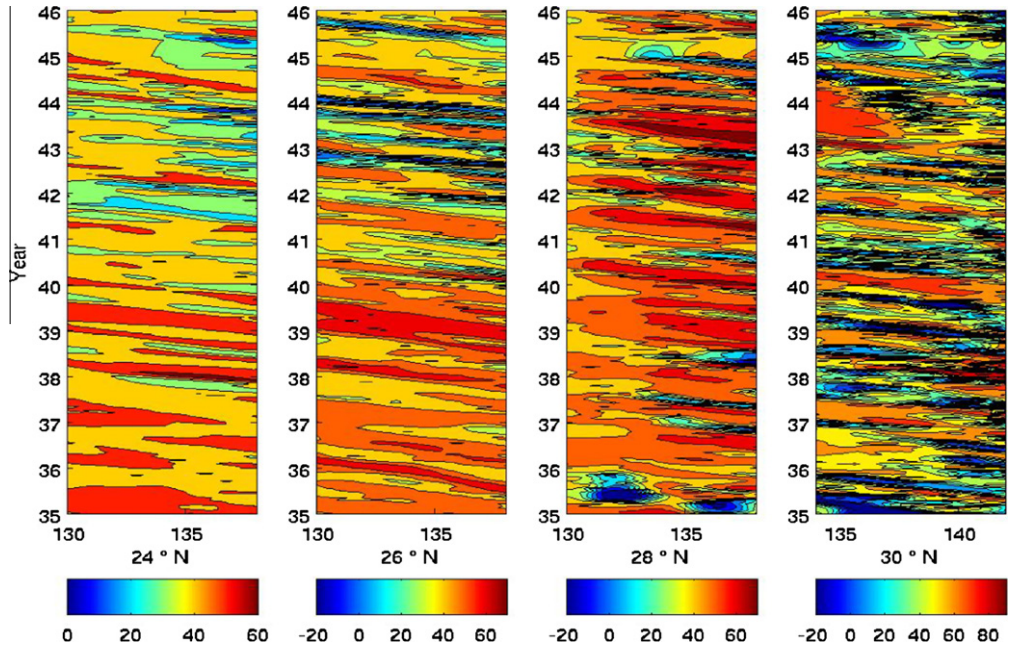

Fig. 20. Hovmoeller plots of SSH anomalies at 24, 26, 28 and 30°N, respectively, from the model year 36–46. The unit is cm.

path through the amplification of this cyclonic eddy. The LM path continues to evolve and forms a large low SSHa through the year. Note that similar small meander processes associated with the cyclonic eddy are commonly seen in the model. The center of the cyclonic anomaly southeast of Kyushu may move meridionally. However, only few of them, similar to those shown in Fig. 19, trigger the formation of the LM and seem to change the Kuroshio east of Japan into the other flow status, while most of them cause the oNLM and dissipate away. The formation process of the LM in the model is quite similar to the typical picture of past LMs (Kawabe, 1995), as occurred in 2004 (Miyazawa et al., 2008). In reality, the meander state can persist over years or decades (Qiu and Miao, 2000).

Earlier studies indicate that all LM paths are formed when the transport in the Tokara Strait increases while the Kuroshio takes an NLM path when the transport is small (e.g., Kawabe, 1995, 2005). LM paths occur when the Kuroshio has large or medium transport and velocity, and is in a northern position in the Tokara Strait, which implies a small curvature and a large vertical inclination of the current axis south of Kyushu. These signatures may be a result of extensive westward propagating eddy interactions southeast of Kyushu. Our results show that the westward propagating anti-cyclonic and cyclonic eddies from the subtropical central Pacific and their interaction affect the meander paths significantly. Fig. 20 shows the Hovmoeller plots of SSHa anomalies at 24, 26, 28 and 30°N, respectively, from the model year 35–46. It is clear that the number of mesoscale eddies which are propagating westward increases with latitude. This is not surprising, since a significant number of eddies are separated from the KE region. Recent studies suggest that the transition between the nNLM and oNLM paths during the last decade is influenced by mesoscale eddy activity (Mitsudera et al., 2001; Ebuchi and Hanawa, 2003). Qiu and Miao (2000) suggested that the accumulation of low potential vorticity water in the Kuroshio recirculation region influences the Kuroshio path variation. Note that the DUPOM is driven by the monthly varying climatological wind forcing. The inter-annual variability exists in the Kuroshio path dynamics and results from the growth of the eddy variability and instability. Our results confirmed that the LM path generation is related to the whole subtropical gyre system, including the low latitudes and recirculation region, rather than a simple local non-linear phenomenon (e.g. Yamagata et al., 1985; Yamagata and Umatani, 1987). The intensive eddy variability indicates that the westward-propagating eddies may play a dominant role (or provide the necessary condition) to trigger the meander path variability and initialize the LM through the flow instability. This comes from the major advantage of DUPOM, in which the intrinsic physical instability is not stabilized by the nature of low numerical viscosity (diffusivity). These westward-propagating eddies have a spatial scale of 300–500 km and a time scale less than 3 months, originating in the KE and entering the Kuroshio recirculation region around 30°N. The meridional variability of KE may also affect the amount of eddy formation. Preliminary analysis shows that slightly shifting the KE northward may reduce the possibilities of the LM path (not shown here) and make the meander paths more stable between nNLM and oNLM. This may be due to the reduced amount of westward-propagating eddies.

6. Conclusions

The current DUPOM model reproduces many important features and circulation patterns in the Asian Marginal Seas, particularly the KCS in the North Pacific. The current results show the strong baroclinic dynamic of the KCS southeast of Japan and provide useful model validation with observation. The multi-scale dynamics of the North Pacific are well simulated using the novel multiple-domains approach, resulting from a robust and energy conservative two-way coupling design.

We can conclude that the strong and northeastward Kuroshio flows principally in the upper layer when it passes the PCM-1 section east of Taiwan. The transport is almost consistent and the main axis varies little, which indicates a stable current flowing through east of Taiwan and into the ECS. A typical cold dome northeast of Taiwan is also resolved by the model, extending from the surface down to the subsurface layer of 60 m deep. The formation process is described in detail here. The main Kuroshio axis continues to flow northeastward and veers at around 30°N, 129°E, turning into the Tokara Strait mostly. A part of the Kuroshio flows into the JES through the Tsushima Strait, known as the Tsushima Warm Current. After passing the strait, the main Kuroshio axis veers again and flows northward to reach the southern coast of Japanese Shikoku. Then it flows northeastward along the southern coast of Japan. Our results also indicate an undercurrent core is observed beneath the Kuroshio near the bottom topography. However, the strength is very weak and the undercurrent is mostly along the continental shelf.

The Kuroshio then leaves Honshu and enters the Pacific as the KE. The model reasonably reproduces different types of Kuroshio path meanders south of Japan and their transient states. The variation of typical meander paths and the formation process of LM are also investigated. Prior to the formation of LM, a small meander was often generated southeast of Kyushu, similar to the observations (Kawabe, 1995; Miyazawa et al., 2008). A cyclonic eddy is trapped between the main Kuroshio axis and the coast. The LM is gradually developed due to the eastward propagation of the cyclonic eddy. In the model, the small meander is often generated southeast of Kyushu but it seldom develops to a LM. The local eddy interaction and regional instability seem to play an important role in triggering the LM. Since the meander path is full of variability both in the model and observation, further investigation is required to clarify the meander path dynamics. Particularly, the interaction between the Kuroshio and westward propagating mesoscale eddies might be the main cause.

Our results show that the present basin-scale DUPOM appears to capture many key elements in the Kuroshio path dynamics and the internal dynamic (including westward propagating eddies) may trigger the variation which could result from the baroclinic instability. Nevertheless, the existence of the different meander states and their transients in the model is worthy of further investigation.

Acknowledgments

The financial support from National Science Council, Taiwan (1002628M002010MY2, and 1002199M001029MY5: Laboratory for Climate Change Research-Consortium for Climate Change Study), is appreciated. We would also like to acknowledge the National Center for High-Performance Computing, Taiwan, for providing computing resources to facilitate this research. Detailed comments from the anonymous reviewers are deeply appreciated.

References

Andres, M., Wimbush, M., Park, J.-H., Chang, K.-I., Lim, B.-H., Watts, D.R., Ichikawa, H., Teague, W.J., http://dx.doi.org/10.1029/2007JC004200, 2008. Observations of Kuroshio flow variations in the East China Sea. Journal of Geophysics Research – Oceans 113, C05013.

Ambe, D., Imawaki, S., Uchida, H., et al., 2004. Estimation the Kuroshio axis south of Japan using combination of satellite altimetry and drifting buoys. Journal of Oceanography 60, 375–382.

Akitomo, K., Kurogi, M., 2001. Path transition of the Kuroshio due to mesoscale eddies: a two-layer, wind-driven experiment. Journal of Oceanography 57, 735–741.

Bingham, F.M., Talley, L.D., 1991. Estimates of Kuroshio transport using an inverse technique. Deep-Sea Research 38, S21–45.
Centurioni, L.R., Niiler, P.P., Lee, D.K., 2004. Observations of inflow of Philippine Sea surface water into the South China Sea through the Luzon Strait. Journal of Physical Oceanography 34, 113–121.
Chern, C.S., Wang, J., 1989. On the water masses at northern off shore area of Taiwan. Acta Oceanographica Taiwanica 22, 14–32.
Chen, C.-T.A., Ruo, R., Paid, S.-C., Liu, C.-T., Wong, G.T.F., 1995. Exchange of water masses between the East China Sea and the Kuroshio off northeastern Taiwan. Continental Shelf Research 15, 19–39.
Chuang, W.-S., Li, H.-W., Tang, T., Wu, C.-K., 1993. Observations of the countercurrent on the inshore side of the Kuroshio northeast of Taiwan. Journal of Oceanography 49, 581–592.
Debreu, L., Blayo, E., 2008. Two-way embedding algorithms: a review. Ocean Dynamics 58, 415–428.
Dietrich, D.E., Mehra, A., Haney, R.L., Bowman, M.J., Tseng, Y.H., 2004. Dissipation effects in North Atlantic Ocean modeling. Geophysical Research Letters 31, L05302.
Dietrich, D.E., Tseng, Y.H., Medina, R., Liste, M., Olabarriet, M., Piacsek, S.A., Bowman, M.J., Mehra, A., http://dx.doi.org/10.1029/2006JC003914, 2008. Accurate Mediterranean overflow water (MOW) simulation using a coupled multiple-grid Mediterranean Sea/North Atlantic Ocean model on a PC. Journal of Geophysics Research – Oceans 113, C07027.
Du, T., Tseng, Y.-H., Yan, X.-H., 2008. Impacts of tidal currents and Kuroshio intrusion on the generation of nonlinear internal waves in Luzon Strait. Journal of Geophysics Research – Oceans 113, C08015.
Ebuchi, N., Hanawa, K., 2003. Influences of mesoscale eddies on variations of the Kuroshio axis. Journal of Oceanography 59, 25–36.
Endoh, T., Hibiya, T., 2000. Numerical study of the generation and propagation of trigger meanders of the Kuroshio south of Japan. Journal of Oceanography 56, 409–418.
Fan, K.L., 1980. On upwelling off northeastern shore of Taiwan. Acta Oceanographica Taiwanica 11, 105–117.
Feng, M., Mitsudera, H., Yoshikawa, Y., 2000. Structure and variability of the Kuroshio current in Tokara Strait. Journal of Physical Oceanography 30, 2257–2276.
Guo, X., Hukuda, H., Miyazawa, Y., Yamagata, T., 2002. A triply nested ocean model for simulating the Kuroshio – roles of horizontal resolution on JEBAR. Journal of Physical Oceanography 33, 146–169.
Hellerman, S., Rosenstein, M., 1983. Normal monthly wind stress over the world ocean with error estimates. Journal of Physical Oceanography 13, 1093–1104.
Hinata, T., 1996. Seasonal variation and long-term trends of the oceanographic conditions along a fixed hydrographic line crossing the Kuroshio in the East China Sea. Oceanography Magazine 45, 9–32.
Hsueh, Y., 2000. The Kuroshio in the East China Sea. Journal of Marine Systems 24, 131–139.
Hurlburt, H.E., Wallcraft, A.J., Schmitz Jr., W.J., Hogan, P.J., Metzger, E.J., 1996. Dynamics of the Kuroshio/Oyashio current system using eddy-resolving models of the North Pacific Ocean. Journal of Geophysics Research – Oceans 101, 941–976.
Ichikawa, H., Chaen, M., 2000. Seasonal variation of heat and freshwater transports by the Kuroshio in the East China Sea. Journal of Marine Systems 24, 119–129.
Ichikawa, H., Beardsley, R.C., 2002. The current system in the Yellow and East China Seas. Journal of Oceanography 58, 77–92.
Imawaki, S., Uchida, H., Ichikawa, H., Fukasawa, M., Umatani, S.I., ASUKA Group, 2001. Satellite altimeter monitoring the Kuroshio transport south of Japan. Geophysical Research Letters 28, 17–20.
Jan, S., Wang, J., Chern, C.-S., Chao, S.-Y., 2002. Seasonal variation of the circulation in the Taiwan Strait. Journal of Marine Systems 35, 249–268.
Johns, W.E., Lee, T.N., Zhang, D., Zantopp, R., Liu, C.T., Yang, Y., 2001. The Kuroshio east of Taiwan: moored transport observations from the WOCE PCM-1 array. Journal of Physical Oceanography 31, 1031–1053.
Kamihira, E., Minami, H., Ishizaki, H., Eguchi, H., Nishizawa, J., 1978. The cut-off phenomenon of the large cold water mass off Tokaido. Bulletin of the Kobe Marine Observatory 195, 1–15 (in Japanese with English abstract).
Kawabe, M., 1980. Sea level variations around the Nansei Islands and the Large Meander in the Kuroshio south of central Japan. Journal of the Oceanographical Society of Japan 36, 227–235.
Kawabe, M., 1985. Sea level variations at the Izu islands and typical stable paths of the Kuroshio. Journal of Oceanography 41, 307–326.
Kawabe, M., 1988. Variability of Kuroshio velocity assessed from the sea-level difference between Naze and Nishinoomote. Journal of the Oceanographical Society of Japan 44, 293–304.
Kawabe, M., 1995. Variations of current path, velocity, and volume transport of the Kuroshio in relation with the Large Meander. Journal of Physical Oceanography 25, 3103–3117.
Kawabe, M., 2005. Variations of the Kuroshio in the southern region of Japan: conditions for Large Meander of the Kuroshio. Journal of Physical Oceanography 61, 529–537.
Kagimoto, T., Yamagata, T., 1997. Seasonal transport variations of the Kuroshio: an OGCM Simulation. Journal of Physical Oceanography 27, 403–418.
Kashima, M., Imawaki, S., Umatani, S., Uchida, H., Hashibe, Y., Ichikawa, H., Fukasawa, M., 2003. Geostrophy in the intermediate and deep layers of the Kuroshio and its recirculation regions south of Japan. Journal of Oceanography 59, 291–301.
Levitus, S., Boyer, T.P., 1994. Temperature, vol. 4. World Ocean Atlas, 1994, NOAA Atlas NESDIS, 117pp.
Lin, C.Y., Shyu, C.Z., Shih, W.H., 1992. The Kuroshio fronts and cold eddies off northeastern Taiwan observed by NOAA-AVHRR imageries. Terrestrial Atmospheric and Oceanic Sciences 3, 225–242.
Liu, C.S., Liu, S.Y., Lallemand, S.E., Lundberg, N., Reed, D.L., 1998. Digital elevation model offshore Taiwan and its tectonic implications. Terrestrial Atmospheric and Oceanic Sciences 9, 705–738.
Masuda, S., Akitomo, K., Awaji, T., 1999. Effects of stratification and bottom topography on the Kuroshio path variation south of Japan. Part I: dependence of path selection on velocity. Journal of Physical Oceanography 29, 2419–2431.
Masuda, S., Akitomo, K., 2000. Effects of stratification and bottom topography on the Kuroshio path variation south of Japan. Part II: path transitions in a multiple equilibrium regime. Journal of Physical Oceanography 30, 1431–1449.
McCreary, J.P., White, W.B., 1979. On a theory of the Kuroshio meander. Deep-Sea Research Part I: Oceanographic Research Papers 26, 317–320.
Mitsudera, H., Waseda, T., Yoshikawa, Y., Taguchi, B., 2001. Anticyclonic eddies and Kuroshio meander formation. Geophysical Research Letters 28, 2025–2028.
Miyazawa, Y., Kagimoto, T., Guo, X., Sakuma, H., http://dx.doi.org/10.1029/2007JC004226, 2008. The Kuroshio Large Meander formation in 2004 analyzed by an eddy-resolving ocean forecast system. Journal of Geophysics Research – Oceans 113, C10015.
Nishida, H., 1982. Description of the Kuroshio meander in 1975–1980—Large meander of the Kuroshio in 1975–1980 (I). Report of Hydrographic Research, Tokyo 17, 181–207.
Nitani, H., 1972. Beginning of the Kuroshio. In: Stommel, H., Yoshida, K. (Eds.), Kuroshio—Its Physical Aspects. Univ. Tokyo Press, Tokyo, pp. 129–163.
Nagata, Y., Takeshita, K., 1985. Variation of the sea surface temperature distribution across the Kuroshio in the Tokara Strait. Journal of the Oceanographical Society of Japan 41, 244–258.
Oka, E., Kawabe, M., 1998. Characteristics of variations of water properties and density structure around the Kuroshio in the East China Sea. Journal of Oceanography 54, 605–617.
Oka, E., Kawabe, M., 2003. Dynamic structure of the Kuroshio south of Kyushu in relation to the Kuroshio path variations. Journal of Oceanography 59, 595–608.
Pacanowski, R.C., Philander, S.G.H., 1981. Parameterization of vertical mixing in numerical models of tropical oceans. Journal of Oceanography 11, 1443–1451.
Qiu, B., Miao, W., 2000. Kuroshio path variations south of Japan: bimodality as a self-sustained internal oscillation. Journal of Physical Oceanography 30, 2124–2137.
Saiki, M., 1982. Relation between the geostrophic flux of the Kuroshio in the Eastern China Sea and its large-meanders in south of Japan. Oceanography Magazine 32, 11–18.
Shen, M.L., Tseng, Y.-H., Jan, S., 2011. The formation and dynamics of cold-dome off northeastern Taiwan. Journal of Marine Systems 86, 10–27.
Taft, B., 1972. Characteristics of the flow of the Kuroshio south of Japan. In: Stommel, H., Yoshida, K. (Eds.), Kuroshio—Its Physical Aspects. Univ. of Tokyo Press, Tokyo. pp. 165–216.
Tang, T.Y., Tai, J.H., Yang, Y.J., 2000. The flow pattern north of Taiwan and the migration of the Kuroshio. Continental Shelf Research 20, 349–371.
Tseng, Y.H., Dietrich, D.E., Ferziger, J.H., http://dx.doi.org/10.1029/2007JC004093, 2005. Regional circulation of the Monterey Bay region: hydrostatic versus nonhydrostatic modeling. Journal of Geophysics Research – Oceans 110, C09015.
Tseng, Y.H., Jan, S., Dietrich, D.E., Lin, I.-I., Chang, Y.T., Tang, T.Y., 2010. Modeled oceanic response and sea surface cooling to typhoon Kai-Tak. Terr. Atmos. Ocean. Sci. 21, 85–98.
Tseng, Y.H., Chien, M.H., 2011. Parallel Domain-decomposed Taiwan Multi-scale Community Ocean Model (PD-TIMCOM). Computers and Fluids 45, 77–83.
Usui, N., Tsujino, H., Fujii, Y., et al., http://dx.doi.org/10.1029/2007JC004266, 2008. Generation of a trigger meander for the 2004 Kuroshio Large Meander. Journal of Geophysics Research 113, C01012.
Waseda, T., Mitsudera, H., 2002. Chaotic advection of the shallow Kuroshio coastal waters. Journal of Oceanography 58, 627–638.
Wu, R., Kirtman, B.P., Pegion, K., 2006. Local air–sea relationship in observations and model simulations. Journal of Climate 19, 4914–4932.
Yin, F., 1973. Preliminary study of cold water mass near N.N.E. of Taiwan. Acta Oceanographica Taiwanica 3, 157–180.
Yamagata, T., Shibao, Y., Umatani, S., 1985. Interannual variability of the KE and its relation to the Southern Oscillation/El Nino. Journal of the Oceanographical Society of Japan 41, 274–281.
Yamagata, T., Umatani, S., 1987. The capture of current meander by coastal geometry with possible application to the Kuroshio current. Tellus 39, 161–169.
Yamamoto, H., Ando, K., Misumi, A., 1993. Estimation of Kuroshio Volume Transport in the East China Sea—Based on Kuroshio Cruise in Oct. 1989, in Oct. 1990 and in Oct. 1991. Japan Marine Science and Technology Center Rep. 30, pp. 37–59 (in Japanese with English abstract).
Yamamoto et al., 1998. Variability of Kuroshio Current in the Tokara Strait. Japan Marine Science and Technology Center Rep. 37, 45pp.
Yoshinari, H., Ikeda, M., Tanaka, K., Masumoto, Y., 2004. Sensitivity of the interannual Kuroshio Transport variation south of Japan to wind dataset in OGCM calculation. Journal of Oceanography 60, 341–350.
Young, C.C., Tseng, Y.H., Shen, M.L., Liang, Y.C., Chien, M.H., Chien, C.H., http://dx.doi.org/10.1016/j.envsoft.2012.05.017, 2012. Software development of the Talwan Multi-scale Community Ocean Model (TIMCOM). Environmental Modelling and Software.

Yuan, Y., Kaneko, A., Su, J., Zhu, X., Liu, Y., Gohda, N., Chen, H., 1998. The kuroshio east of taiwan and in the east china sea and the currents east of Ryukyu islands during early summer of 1996. Journal of Oceanography 54, 217–226.

Zang, Y., Street, R.L., Koseff, J.R., 1994. A non-staggered grid, fractional step method for time-dependent incompressible Navier–Stokes equations in curvilinear coordinates. Journal of Computational Physics 114, 18–33.

Zhang, D., Lee, T.N., Johns, W.E., Liu, C.T., Zantopp, R., 2001. The Kuroshio east of Taiwan: modes of variability and relationship to interior ocean meso-scale eddies. Journal of Physical Oceanography 31, 1054–1074.

Zhu, X.H., Park, J.H., Kaneko, I., 2006. Velocity structures and transports of the Kuroshio and the Ryukyu current during Fall of 2000 estimated by an inverse technique. Journal of Oceanography 62, 587–596.